Structural and Geochronological Constraints on Devonian Suprasubduction Tectonic Switching and Permian Collisional Dynamics in the Chinese Altai, Central Asia

Y. D. Jiang[1,2] , K. Schulmann[3,4], M. Sun[5], R. F. Weinberg[6] , P. Štípská[3,4], P. F. Li[1] , J. Zhang[7], F. Chopin[3,4], S. Wang[1], X. P. Xia[1] , and W. J. Xiao[8]

[1]State Key Laboratory of Isotope Geochemistry, Guangzhou Institute of Geochemistry, Chinese Academy of Sciences, Guangzhou, China, [2]Chinese Academy of Sciences, Institutions of Earth Science, Beijing, China, [3]Czech Geological Survey, Praha, Czech Republic, [4]EOST, Institut de Physique du Globe, UMR 7516, Université de Strasbourg, Strasbourg, France, [5]Department of Earth Sciences, The University of Hong Kong, Hong Kong, [6]School of Earth, Atmosphere and Environment, Monash University, Clayton, Victoria, Australia, [7]School of Earth Science and Geological Engineering, Sun Yat-sen University, Guangzhou, China, [8]Division of Tethys Research Center, Institute of Geology and Geophysics, Chinese Academy of Sciences, Beijing, China

Abstract Kinematic significance and time scales of geodynamic processes forming the Altai Orogenic Belt are addressed through structural and petrological analysis combined with zircon and monazite geochronology. The study area is composed of orogenic lower crust represented by a Devonian migmatite-magmatite complex and orogenic middle and upper crust formed by an amphibolite-facies Ordovician sedimentary sequence and a weakly to unmetamorphosed Devonian volcano-sedimentary cover, respectively. The orogenic lower and middle crust were first affected by moderate thickening, which formed subhorizontal Barrovian metamorphic schistosity. This fabric was reworked by deep crustal melting and intrusion of granite sheets during horizontal extension at 400–380 Ma. Soon after, this horizontal fabric was affected by NW-SE shortening generating crustal-scale upright folding associated with subvertical flow of still partially molten orogenic lower crust. During this event, the orogenic lower and middle crust were tightly juxtaposed with upper crustal sedimentary rocks. The last event was related with a NE-SW oriented convergence resulting in large-scale folding and megafold interference pattern in the Permian at 280–273 Ma. Combined with existing regional data, our results allow proposing a Devonian tectonic switching from compression to extension and back to compression, as a response to variations of subduction dynamics between slab advance and retreat in a Pacific-type suprasubduction system. The Permian folding was associated with the progressive northward exhumation of thermally softened crust. This tectonic evolution is in response to the indentation of the rigid Junggar arc domain into the weak Altai wedge.

1. Introduction

Long-lasting Pacific-type convergence forms giant accretionary orogens by amalgamations of voluminous island arcs, seamounts, accretionary wedges, and microcontinents to continental nuclei (Cawood et al., 2009). The evolution of accretionary orogens may involve multiple amalgamation of terranes, variable block rotation, oroclinal bending, and strike-slip duplication, generating vast complexity of the crustal architecture (Şengör & Natal'in, 1996; Şengör et al., 1993; Xiao et al., 2018). In addition, multiple magmatic, sedimentary additions and alternation of metamorphic events characterized by middle-pressure/middle-temperature and low-pressure/high-temperature conditions can be generated due to tectonic switching resulted from variations in subduction dynamics from advancing to rollback modes (Collins, 2002; Collins & Richards, 2008). Accretionary orogens may eventually evolve into collisional ones as their active subduction systems are gradually brought to a halt by the arrival of large buoyant continental blocks that act as stoppers in the subduction zone (e.g., Schulmann & Paterson, 2011). Later collisional processes may lead to superposed folding events, partial or complete structural and metamorphic reworking of early accretionary structures, and large-scale recycling by syntectonic to posttectonic magmatism (e.g., Collins et al., 2011; Tian et al., 2013). The reconstruction of the finite architecture of fossil accretionary orogens is thus often complicated.
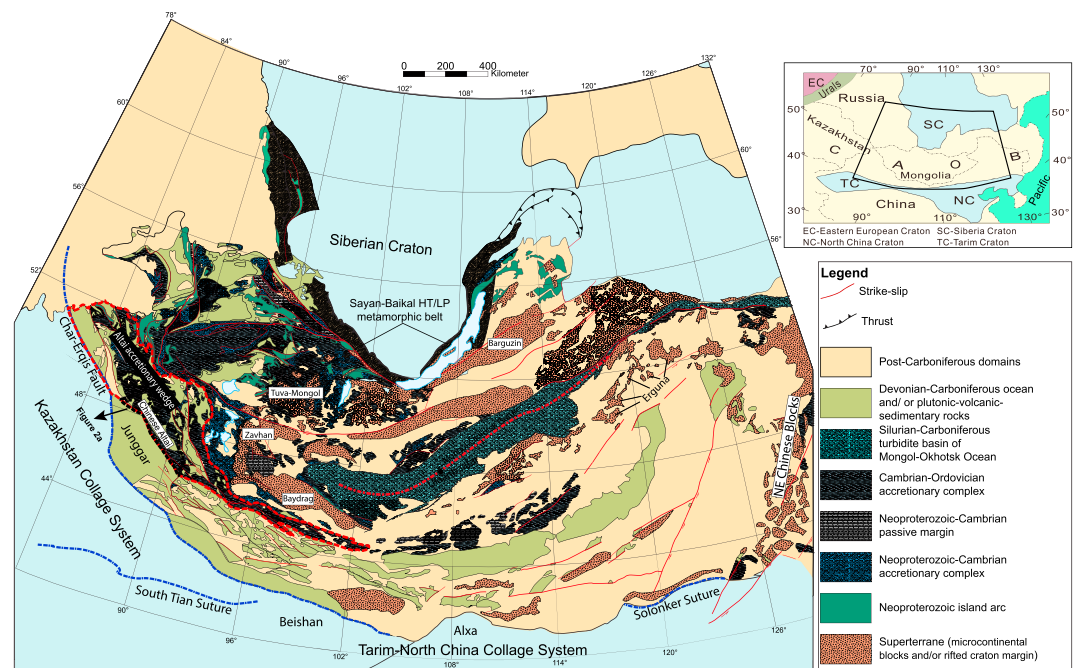
Figure 1. Simplified geological map of the Mongolian Collage System (modified from Jiang et al., 2017). Extent of the Altai accretionary wedge and the location of the Chinese Altai are outlined by dashed lines. Inset shows the position of the Central Asian Orogenic Belt.

The Central Asian Orogenic Belt (CAOB) was shaped by a long-lasting accretion and a subsequent collision (e.g., Windley et al., 2007; Xiao et al., 2015). However, the tectonic process accounting for the transition from accretion to collision has been so far poorly described. Here we focus on the Altai accretionary wedge, which represents a key component of the Mongolian Collage forming an eastern tract of the CAOB (Figure 1; Şengör et al., 1993; Windley et al., 2007). This wedge represents an ~1,500 km long early Paleozoic volcano-sedimentary accretionary prism rimming the active margin of the Mongolian Precambrian blocks (Jiang et al., 2017). The wedge was transformed into a mature orogenic system during the Devonian-Carboniferous (420–360 Ma) Altai orogeny associated with extensive magmatism and synchronous metamorphism (e.g., Cai, Sun, Yuan, Long, et al., 2011; Jiang et al., 2010; Wang et al., 2006). A second, less extensive Permian tectonothermal event is increasingly reported and evidenced by a large amount of ages ranging from 290 to 250 Ma derived from zircon and monazite U-Pb and ^{40}Ar/^{39}Ar dating of K-bearing minerals (e.g., Briggs et al., 2007; Laurent-Charvet et al., 2003; Li et al., 2017; Zhang et al., 2012). This event was interpreted as a consequence of either postcollisional extension (Tong et al., 2014; Wang et al., 2014) or compression related to the amalgamation of the Altai accretionary wedge with southerly Junggar arc domain (Briggs et al., 2007; Broussolle et al., 2018; Li, Sun, Rosenbaum, Cai, et al., 2016; Li et al., 2017; Zhang et al., 2012).

As mentioned above, the Devonian and Permian tectonic events played important roles in the transformation of the primary volcano-sedimentary accretionary wedge into the mature Altai orogenic belt. However, to date, our knowledge of its tectonic evolution is mainly derived from geochemical and geochronological studies. Structural data in the region are restricted to the southerly Erqis fault zone that was deeply affected by the Permian event. The existence of Devonian structures could be partly deduced from structural restorations (Jiang et al., 2015; Zhang et al., 2015); however, their geometries and related structural evolution remain poorly constrained. To further address the complexity of Altai orogenic processes, we examine the structural and metamorphic evolution of both the Ordovician and Devonian sequences and the deep crustal migmatite-magmatite complex, thus covering different exposed orogenic crustal levels of the Altai orogen. The timing of the tectonometamorphic events of the whole edifice is constrained by zircon and monazite U-Pb dating of selected metamorphic and magmatic/volcanic rocks. Structural and petro-chronological data are then synthetized in order to discriminate geometries, kinematics of individual fabrics, and assign them Devonian or Permian ages. By doing this, we provide a fully constrained deformation time scheme of the

accretionary-collisional evolution portrayed in a synthetic evolutionary model of 3-D architecture of the Altai crust.

2. Geological Setting

2.1. Regional Geological Background

The CAOB, also known as Altaides, extends from the Ural Mountains in the west to the Pacific Ocean in the east and from the Siberian and East European Cratons in the north to the North China and Tarim Cratons in the south (Figure 1; Mossakovsky et al., 1993; Şengör et al., 1993). It has been shown that this giant orogenic belt was formed by a stepwise accretion of island arcs, ophiolites, oceanic islands, seamounts, accretionary wedges, and microcontinents to the Siberian Craton in the north from the Late Proterozoic to Permian (Kröner et al., 2007; Wilhem et al., 2012; Windley et al., 2007). Xiao et al. (2015) proposed a subdivision of the CAOB into three main collage systems: the Mongolian Collage in the east, the Kazakhstan Collage in the west, and the Tarim-North China Collage in the south (Figure 1). Geologically, the Mongolian Collage is limited by the early Paleozoic Sayan-Baikal metamorphic belt rimming the southern margin of the Siberian Craton in the north (Donskaya et al., 2000; Gladkochub et al., 2008) and by the late Permian to Early Triassic Solonker suture zone bordering the northern margin of the North China Craton in the south (Xiao et al., 2003). The 2,000-km-long Char-Erqis fault zone is considered by some authors as the southwestern limit of the Mongolian Collage (e.g., Xiao et al., 2015). The Mongolian Collage itself consists of the accreted Mongolian Precambrian blocks overthrust by late Proterozoic ophiolites and accretionary wedge during a main Early Cambrian accretionary event (Buriánek et al., 2017; Jiang et al., 2017). The Proterozoic wedge was intruded by an ~1,800-km-long Cambro-Ordovician Ikh-Mongol arc system (e.g., Janoušek et al., 2018).

Further south occurs a giant Late Cambrian to Ordovician volcano-sedimentary unit stretching from Russia to central Mongolia. It is dominated by terrigenous clastic sedimentary components with subordinate volcanogenic tuffaceous layers, imbricated with dismembered ophiolites (Badarch et al., 2002; Safonova et al., 2009; Xiao et al., 2009). The sedimentary components are chemically immature, compositionally analogous to graywacke, and marked by significant input of felsic to intermediate arc components (Chen et al., 2014; Helo et al., 2006; Jiang et al., 2012; Long et al., 2008; Sun et al., 2008). The lithological content of this unit led Xiao et al. (2009) to interpret it as a giant "Altai" accretionary wedge. Together with the Ikh-Mongol arc system (Janoušek et al., 2018), it represents a huge early Paleozoic Altai accretionary system, rimming the active margin of the Precambrian Zavhan and Baydrag ribbon continents to the northeast (Figure 1; Jiang et al., 2017; Soejono et al., 2018). This accretionary system developed above a long-lasting and retreating Pacific-type oceanic plate that produced Devonian to Carboniferous oceanic assemblages further south (Jiang et al., 2017; Nguyen et al., 2018; Xiao et al., 2009). In the Chinese Altai, the structurally deepest Ordovician sedimentary sequence of the wedge is called the Habahe Group that represents the oldest lithological unit in the region. The Habahe Group is unconformably covered by Devonian sedimentary sequences composed of the volcano-clastic Kangbutiebao Formation and the turbiditic Altai Formation (Windley et al., 2002).

2.2. Overview of Devonian and Permian Tectonothermal Events in the Chinese Altai

The Devonian tectonothermal events revealed mostly by geochronological studies of granitoids cover about 40% of the map surface of the region (Zou et al., 1988). More than 90% of these granitoids have been emplaced during Late Silurian to Middle Devonian (420 to 370 Ma) with a peak of zircon crystallization ages at ca. 400–390 Ma (Cai, Sun, Yuan, Long, et al., 2011; Yuan et al., 2007). Geochemically, these granitoids exhibit both I- and S-type affinities and were considered as products of synorogenic arc magmatism (Cai, Sun, Yuan, Long, et al., 2011; Wang et al., 2006; Yuan et al., 2007), interpreted to result from Silurian-Devonian long-lasting subduction (Wang et al., 2006). Coeval with the peak age of this major magmatism, a regional Middle Devonian anatexis event was revealed by U-Pb dating of metamorphic zircons of migmatitic gneisses from several parts of the Chinese Altai (Jiang et al., 2010). Jiang et al. (2016) further showed that there exists a close temporal and spatial relationship between the regional anatexis of the Habahe Group and the formation of the Devonian granitoids, as well as geochemical similarities between them. These authors proposed that the Devonian granitoids could have originated by anatexis of chemically primitive Habahe Group resulting in the formation of the vertically stratified continental crust of the Chinese Altai. Such a stratified crust was subsequently affected by large-scale upright folds of presumably Middle-
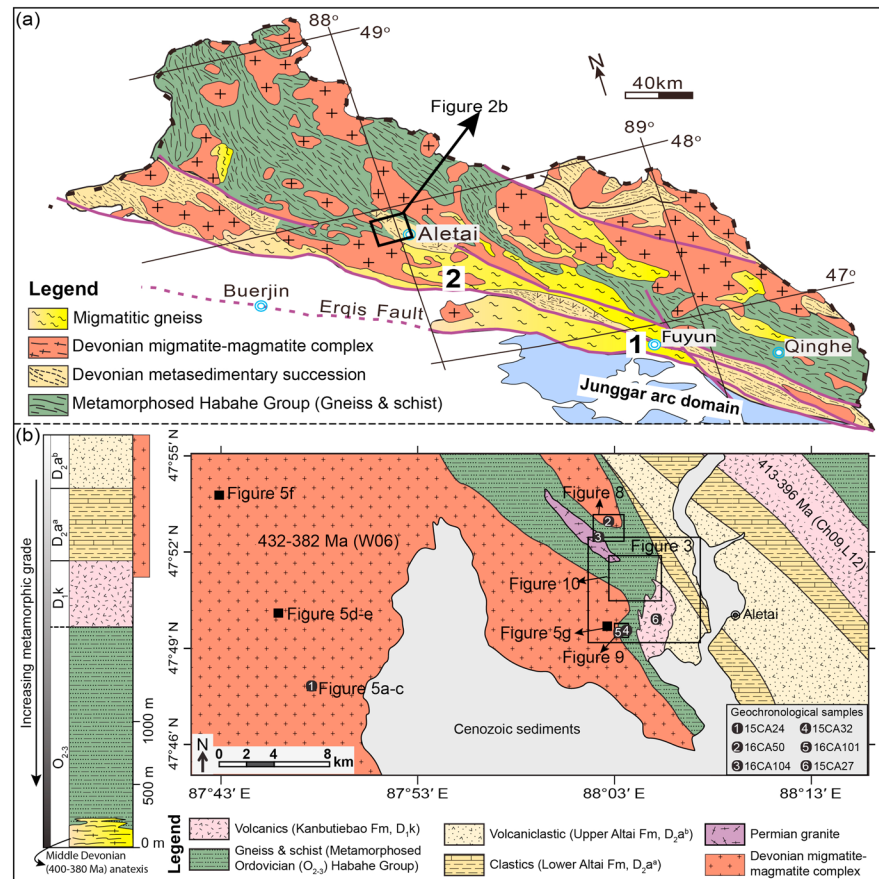
Figure 2. (a) Geological map of the Chinese Altai showing the main lithological units (modified after Jiang et al., 2015). (b) Geological map of the area studied. Major lithological units and their magmatic or deposition ages are correlated in a generalized lithostratigraphic column. Zircon U-Pb ages shown in the map are from Wang et al. (2006) labeled "W06" and Chai et al. (2009) and Liu et al. (2012), labeled "Ch09, L12." Metamorphic conditions of principal units are indicated in the lithotectonic column. Positions of Figures 3, 5a–5g, 8, 9, and 10 and sample locations are indicated.

Late Devonian ages responsible for the formation of large granite-migmatite domes reported from the western part of the Chinese Altai (Jiang et al., 2015; Zhang et al., 2015). A Barrovian tectonometamorphic event was defined in the Buerjin area further NW and is represented by a metamorphic, generally gently inclined schistosity (Jiang et al., 2015). The age of this earliest event is currently unknown, but based on relationships between later granitoids and the Barrovian metamorphic zoning in the adjacent Mongolian Altai (e.g., Burenjargal et al., 2014), it could be considered to be of pre-Devonian age (Jiang et al., 2015).

The Permian event is characterized by volumetrically small late Paleozoic granitoids and gabbroic bodies with emplacement U-Pb zircon ages ranging from 300 to 270 Ma (e.g., Zhang et al., 2014). These rocks are spatially concentrated along the southern flank of the Chinese Altai (T. Wang et al., 2009; Zhang et al., 2014). The granitoids have an A-type chemical affinity and were interpreted as a result of anorogenic magmatism related to postorogenic extension (Cai, Sun, Yuan, Zhao, et al., 2011). Abundant Permian metamorphic zircon and monazite U-Pb ages ranging from 290 to 260 Ma were reported in recent years (Briggs et al., 2007; Zheng et al., 2007). These ages are believed to date the timing of the low-pressure/(ultra) high-temperature metamorphism, characterized by the mineral assemblage sillimanite, spinel, orthopyroxene, and garnet-cordierite (Li et al., 2014; Tong et al., 2014; W. Wang et al., 2009) and are interpreted as a result of either lithospheric extension during Permian (e.g., W. Wang et al., 2009) or plume activity (e.g., Tong et al., 2014).

There are two areas of Permian deformation and metamorphism that have been extensively studied during the last decade. The first area is the NW-SE trending Erqis fault zone near the Fuyun city, where the migmatites and paragneisses of the Chinese Altai occur in direct contact with folded Junggar Carboniferous strata to the south ("Zone 1" in Figure 2a). Briggs et al. (2007) studied deformational

structures in this zone, which are consistent with contractional deformation and top-to-south thrusting. Li, Sun, Rosenbaum, Cai, et al. (2016) and Li et al. (2017) proposed that the region was affected by partitioned transpressional deformation resulting in formation of regional-scale upright folds and sinistral shear zones. Crustal anatexis was dated by U-Pb dating of zircons from leucosomes at 295 Ma (Li et al., 2017) and 283 Ma (Zhang et al., 2012). These ages are broadly consistent with a metamorphic zircon U-Pb age of 277 Ma from an adjacent pelitic granulite (Li et al., 2014) and an in situ monazite U-Th-Pb age of ca. 280 Ma from an adjacent high-grade schist (Briggs et al., 2007). The second most studied area is the Kalasu zone, SE of the Altai city ("Zone 2" in Figure 2a). This NW-SE trending zone consists of Early Permian (U) HT granulites and migmatites surrounded by medium- to low-grade Habahe Group metasedimentary rocks and Devonian volcanoclastic rocks (e.g., Tong et al., 2014; W. Wang et al., 2009). A combined structural and geochronological study by Broussolle et al. (2018) showed a vertical and tabular deformation zone in the center of the area, along which migmatites and granulites were extruded accompanied by important upright folding. Here U-Pb zircon geochronology yielded an age of ca. 299 Ma for migmatite leucosomes (Broussolle et al., 2018) and 292 Ma (W. Wang et al., 2009) and ca. 280 Ma for metapelitic granulite (Tong et al., 2013). Migmatite and granulite in the core of the extrusion zone were later intruded by gabbros and granites, which were dated 284–280 Ma by U-Pb zircon method (Broussolle et al., 2018).

2.3. Geology of the Study Area

This study focuses on a region SW of the Altay city (Figure 2a). This critical area covers all the key lithological and metamorphic sequences known from western Chinese Altai that are from structurally deep to shallow levels: (1) high-grade migmatite-magmatite complex, (2) a metamorphosed, but not migmatized, Ordovician sedimentary sequence (the Habahe Group), and (3) a weakly to unmetamorphosed volcanoclastic sedimentary Devonian succession.

The migmatite-magmatite complex is composed mainly of granites associated with subordinate migmatitic paragneiss and rare amphibolite. The granites are essentially of two major types: medium- to coarse-grained two-mica granites and texturally inhomogeneous schlieren-rich granites. Previous zircon U-Pb studies on granites from this complex indicate that magmatic activity mostly occurred intermittently from 432 to 382 Ma, with a dominant peak at ca. 400 Ma (Cai, Sun, Yuan, Long, et al., 2011; Tong et al., 2007; Wang et al., 2006). The migmatitic paragneisses are stromatitic to nebulitic and structurally correspond to partially molten Habahe Group rocks that have been reported from other parts of the Chinese Altai (Jiang et al., 2015, 2011). Apart from this main migmatite-magmatite complex, small oval-shaped granite bodies locally intruded into the metamorphosed Ordovician Habahe Group.

The metamorphosed Ordovician Habahe Group consists mainly of amphibolite-facies coarse-grained mica schist interlayered with quartzo-feldspathic rocks and quartzites. This sequence was affected by both Barrovian- and Buchan-type metamorphism, characterized by the juxtaposition of middle-pressure/middle-temperature staurolite-kyanite bearing and low-pressure/high-temperature andalusite-bearing metamorphic assemblages (Wei et al., 2007). It has been suggested that the Barrovian series minerals (staurolite and kyanite) were reequilibrated during the Buchan-type (sillimanite-andalusite) metamorphic overprint (Wei et al., 2007). This is further supported by microstructural observations indicating that the kyanite and staurolite grew earlier than andalusite (Li, Sun, Rosenbaum, Jiang, et al., 2016). The metamorphic ages for both types of assemblages have so far not been well constrained except for a metamorphic zircon U-Pb age of 299.2 ± 3.4 Ma reported from a sillimanite-bearing gneiss in the highly deformed zone along the contact with the migmatite-magmatite complex ("Permian HT zone" in Figure 3) and interpreted as the timing of Buchan-type metamorphism (Wang et al., 2014).

The Devonian succession unconformably overlying the Habahe Group is made up of volcanic and pyroclastic rocks in the lower part (the Kangbutiebao Formation) and siliciclastic sediments, fossiliferous limestones to volcanoclastic rocks in the upper part (the Altai Formation; Bureau of Geology and Mineral Resources of Xinjiang Uygur Autonomous Region, 1993). Zircons from felsic volcanic rocks of the Kangbutiebao Formation in a neighboring area defined eruption ages clustering around 400 Ma (Chai et al., 2009; Liu et al., 2012).
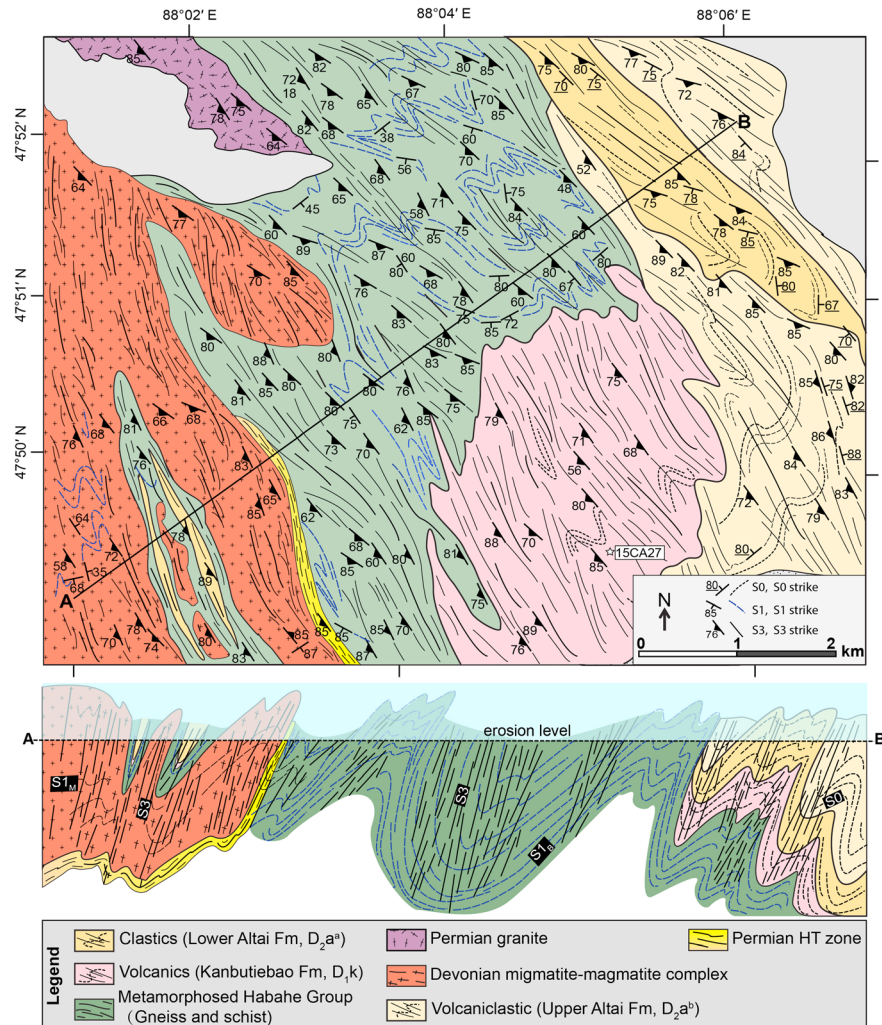
Figure 3. (a) Structural map of planar structures in the studied area showing the distribution and relationship between the early metamorphic foliation $S1_M$ in the migmatite-magmatite complex and the $S1_B$ in the metamorphosed Habahe Group rocks, the sedimentary bedding S_0 in the Devonian sedimentary sequence and the steep S3 fabric. Position of the interpretative profile is also indicated. The extent of the map area and the legend are shown in Figure 2. (b) Structural profile showing the deformational features of the studied area. $S1_B$ represents the earliest metamorphic foliation in the Barrovian-facies rocks, while $S1_M$ represents the earliest macroscopic foliation in the migmatite-magmatite complex.

3. Structural Description

The proximity of the three distinct lithological units makes the studied sequence an ideal area where the relationships between deformation, magmatism, and metamorphism can be closely correlated and understood. Results of detailed structural study are presented in structural maps (Figures 3 and 6), an interpretative cross section (Figure 3), stereonets (Figure 4), and representative structures shown in field photographs (Figures 5, 7, and 8). Three principal deformational episodes (designated D1, D2, and D3) have been identified and are described from structurally deeper to shallower crustal levels.

3.1. Structures of the Migmatite-Magmatite Complex

The granites and various migmatites of this unit show either strong solid-state gneissosity defined by shape-preferred orientation of recrystallized feldspar, quartz, and biotite or magmatic flow fabric defined by alignment of undeformed feldspars and quartz and preferred orientation of restitic schlieren (Figure 5a). These fabrics ($S1_M$) are dominantly subhorizontal or east dipping, bearing east plunging lineation (stereonet in Figure 5b), which are commonly associated with mainly east dipping extensional lock-up shear bands
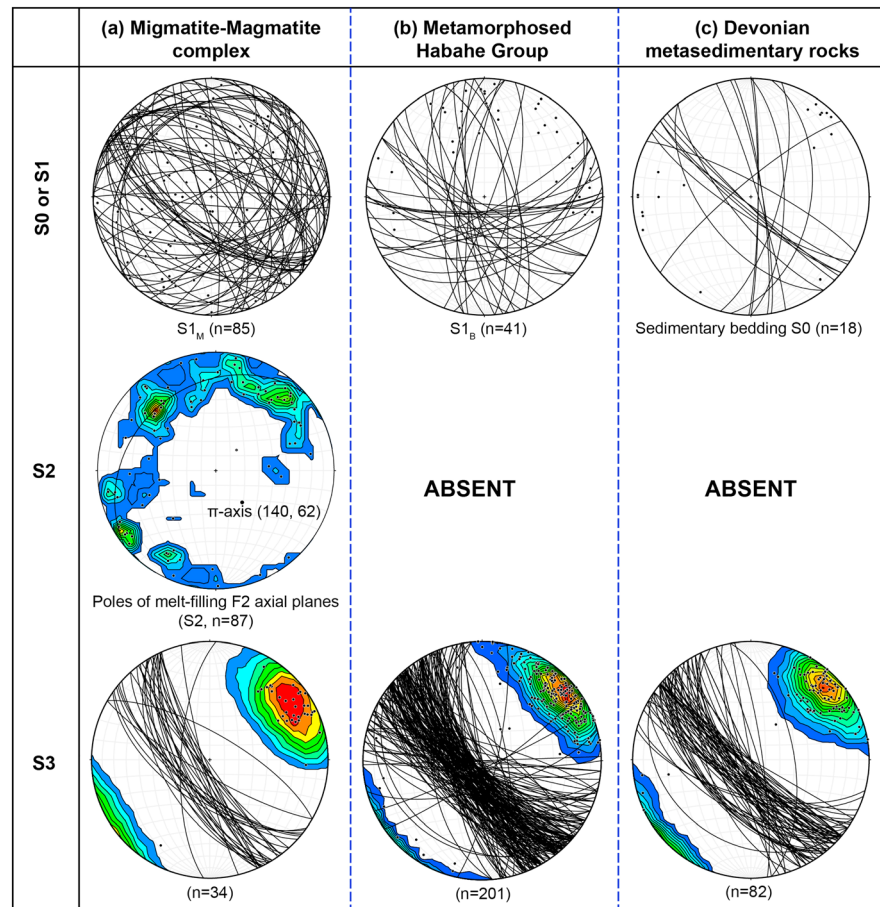
Figure 4. (a–c) Stereonets of poles to planar structures in the studied area.

filled with granitic leucosomes (Figures 5b and 5c, sample 15CA24). These steep to moderately dipping extensional melt-filled shear bands, crosscutting the subhorizontal migmatitic fabric, indicate important vertical shortening and horizontal extension (e.g., Cosgrove, 1997). The $S1_M$ fabric was affected by a second deformation, D2, which rotated the magmatic and migmatitic fabrics $S1_M$ into moderately dipping to subvertical positions (stereonet in Figures 4a and 5d). In some places, the $S1_M$ foliation was transposed by steep S2 fabric in which the $S1_M$-parallel leucosomes are continuously connected to undeformed axial planar leucosomes of F2 folds (Figure 5e). It is therefore difficult to recognize always the $S1_M$ from S2, and the regional high-grade foliation of the migmatite-magmatite complex is referred as a composite $S1$-2_M fabric. This fabric was subsequently affected by D3 deformation and folded by oblique to upright folds (Figures 3 and 5f). These open to close NW-SE trending folds are associated with locally developed subvertical axial planar cleavage (S3, Figure 3 and stereonet in Figure 4a) and in some places with entire transposition of all previous structures. These subvertical S3 cleavages generally developed under greenschist-facies conditions (Figure 5f), in contrast to vertical but high-temperature $S1$-2_M fabrics. However, it is worth noting that a NW-SE trending amphibolite-facies deformation zone developed parallel to the regional S3 foliation, along the contact of the migmatite-magmatite complex with the Ordovician metasedimentary rocks (Figure 5g). This zone is characterized by almost entire transposition of all previously formed structures.

Because of strong D3 transposition, it is difficult to determine the original positions of both the $S1_M$ and $S1$-2_M in the field. However, the poles of the subvertical F2 axial planar leucosome bands (S2) define a great circle with the $\prod$-axis located in the SE sector of the pole figure (140°/62°; Figure 4a) allowing to assess its pre-D3 orientation. The orientation of the $\prod$-axis is close to that of the F3 fold hinges that mainly plunge to the SE under moderate to steep angles (Figure 4a). This implies that the $S1$-2_M foliation dipped dominantly to
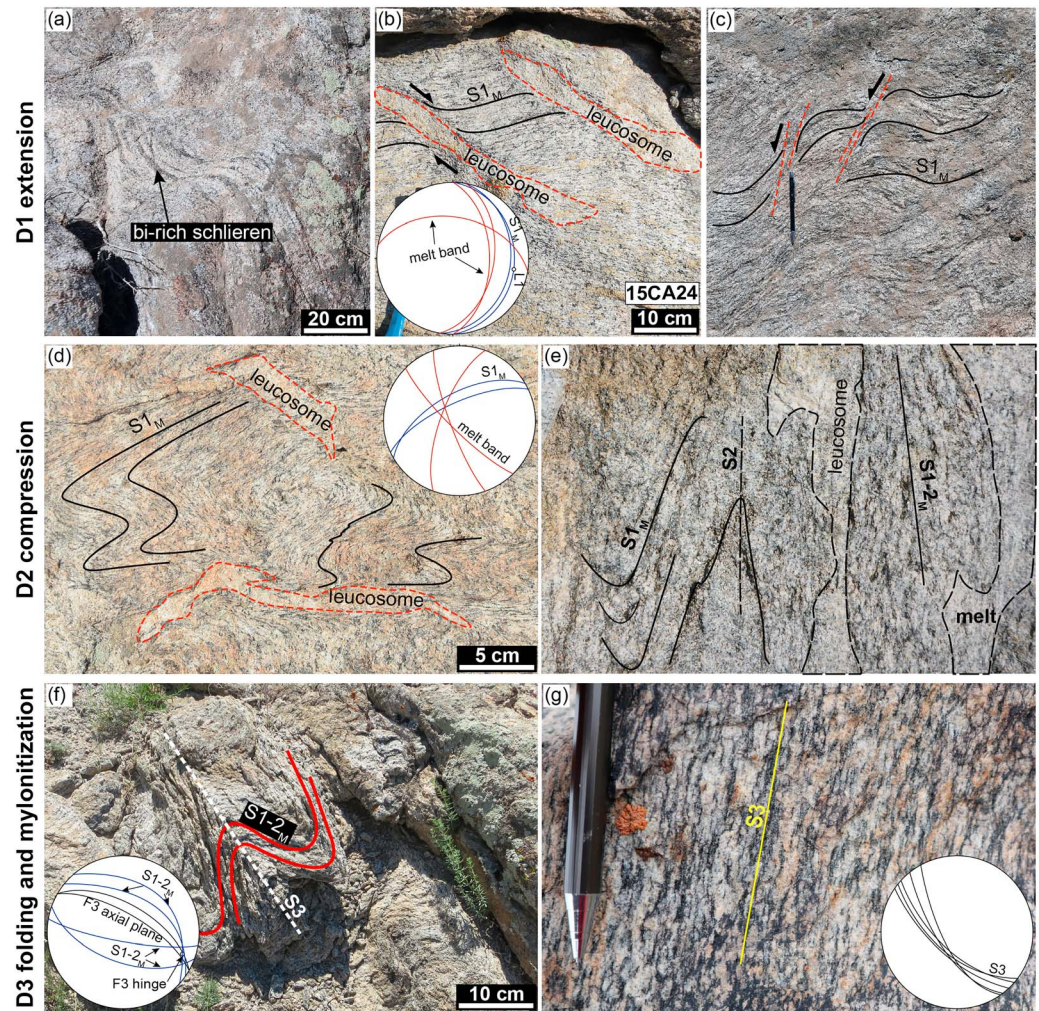
Figure 5. Field photographs illustrating typical structural relationships in the migmatite-magmatite complex. (a) Magmatic fabric (S1$_M$) defined by orientation of restitic Schlieren. (b, c) Migmatitic fabric S1$_M$ is associated with extensional shear bands filled with granitic leucosomes. (d) Transposition of sub-horizontal S1$_M$ foliation by steep melt-bearing S2 foliation and development of axial planar leucosomes of F2 fold. (e) Origin of S1-2$_M$ composite fabric. (f) Character of F3 folding of S1-2$_M$ fabric. (g) Transposition of migmatite-magmatite fabric by mylonitic S3 foliation along the contact with the metamorphosed Habahe Group.

the SE prior the D3 reworking. In addition, the hinges of F3 folds also form a main SE plunging maximum and a subordinate NW plunging maximum, thereby forming a NW-SE trending great circle in the stereonet (Figure 6). This great circle defines a horizontal SW-oriented $\prod$-axis (227°/2°; Figure 6) suggesting that the S1 foliation was originally subhorizontal before being folded by the NE-SW striking F2 folds and/or transposed by the S2 fabric.

3.2. Structures of the Metamorphosed Habahe Group

The metamorphosed Habahe Group rocks show a comparable deformational pattern to the structurally deeper migmatite-magmatite complex. Here a bedding-parallel foliation S1$_B$, defined by alternation of quartz-rich and mica-rich layers, is the dominant structure (Figure 7a). In contrast to migmatites, it is difficult to retrieve the D2 deformation in the field. The upright F2 folds are only locally preserved, and they are extensively refolded by F3 folds (Figure 7b). No features typical for fabric transposition associated with the D2 deformation were observed. However, the existence of the F2 folding can be partly deduced from highly variable orientation of the S1$_B$ foliations (Figures 3 and 4) and partly from distribution of the F3 fold axes (Figure 6). The D2 deformation is thus responsible only for the reorientation of the S1$_B$ fabric, but it is not associated with development of penetrative metamorphic foliation.
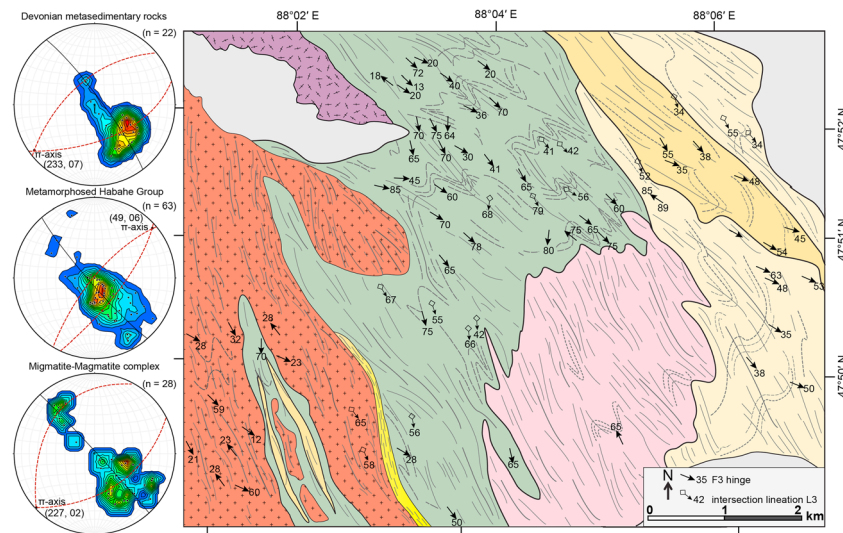
Figure 6. Structural map of lineations and fold hinges of the studied area; for legend see Figure 3. Stereonets show F3 fold axes plunging either to the SE or NW and defining a great circle with ∏-axes plunging gently NE. Trajectories of planar structures correspond to those in Figure 3. Idealized positions of pre-D3 folding planar structures indicated in stereonets of F3 fold axes.

The $S1_B$ metamorphic foliation was affected by upright NW-SE trending folds F3 with subvertical axial planes and fold hinges moderately to steeply plunging either to SE or NW (Figures 6, 7b, and 7c). The folding is associated with development of subvertical S3 cleavage dipping predominantly to the NE (Figure 3 and stereonet in Figure 4b). When plotted on the stereonet, the F3 fold axes tend to define a great circle with subhorizontal NE plunging ∏-axis (49°/6°; Figure 6). This pattern, similar to the migmatite-magmatite complex, implies that prior to D3, the S1 fabric dipped either to the SE or to the NW, which is consistent with the existence of tight and upright NE-SW trending F2 folds with subhorizontal hinges, which in turn folded the subhorizontal S1 fabric. In addition, a small garnet-bearing granite intrusion, located in the north of the study area, crosscuts the $S1_B$ of the metamorphosed Habahe Group (Figures 2, 8a, and 8b). This granite developed a strong subsolidus fabric that is parallel to the S3 foliation in the metamorphosed Habahe Group (Figure 8c). We also note that the strikes of global S3 foliations were gently rotated from NW-SE to NNW-SSE in the western part of the study area, possibly as a result of later processes, such as drag folding or perturbation of the strain field generated by the presence of an irregular, rigid migmatite-magmatite body.

3.3. Structures of the Devonian Sedimentary Succession

The overlying Devonian sedimentary rocks are weakly metamorphosed and show well-preserved sedimentary bedding (S0) oriented obliquely with respect to the subvertical axial planar cleavage S3 of meter to hundred meter scale, NW-SE trending buckle F3 folds (Figures 3, 4, and 7e–7g).

The D3 deformation is heterogeneous and results in alternation of domains dominated by zones of cleavage and zones of asymmetrical folds that rotate the S0 bedding planes toward parallelism with their long limbs (Figure 3). Like in the underlying metamorphosed Habahe Group rocks and the structurally deepest migmatite-magmatite complex, the F3 fold axes plunge mainly to the SE at moderate angles (Figure 6). When plotted on the stereonet, the F3 fold axes define a great circle with a subhorizontal or gently SW plunging ∏-axis (233°/7°; Figure 6). All that implies that prior the D3 deformation, the S0 surfaces were folded by upright NE-SW trending F2 folds and that the S0 bedding was subhorizontal before the F2 folding. These geometrical relationships are similar to those reported from the migmatite-magmatite complex and the metamorphosed Habahe Group.

3.4. Structures of Late Pegmatite Dykes and Granite

Many pegmatite bodies intruded mainly the Habahe Group metasedimentary sequence and its adjacent migmatite-magmatite complex (Figure 9a). The pegmatites consist of quartz, muscovite, microcline, plagioclase, and garnet and form centimeter to meter wide, and several meters up to 1-km-long dykes.
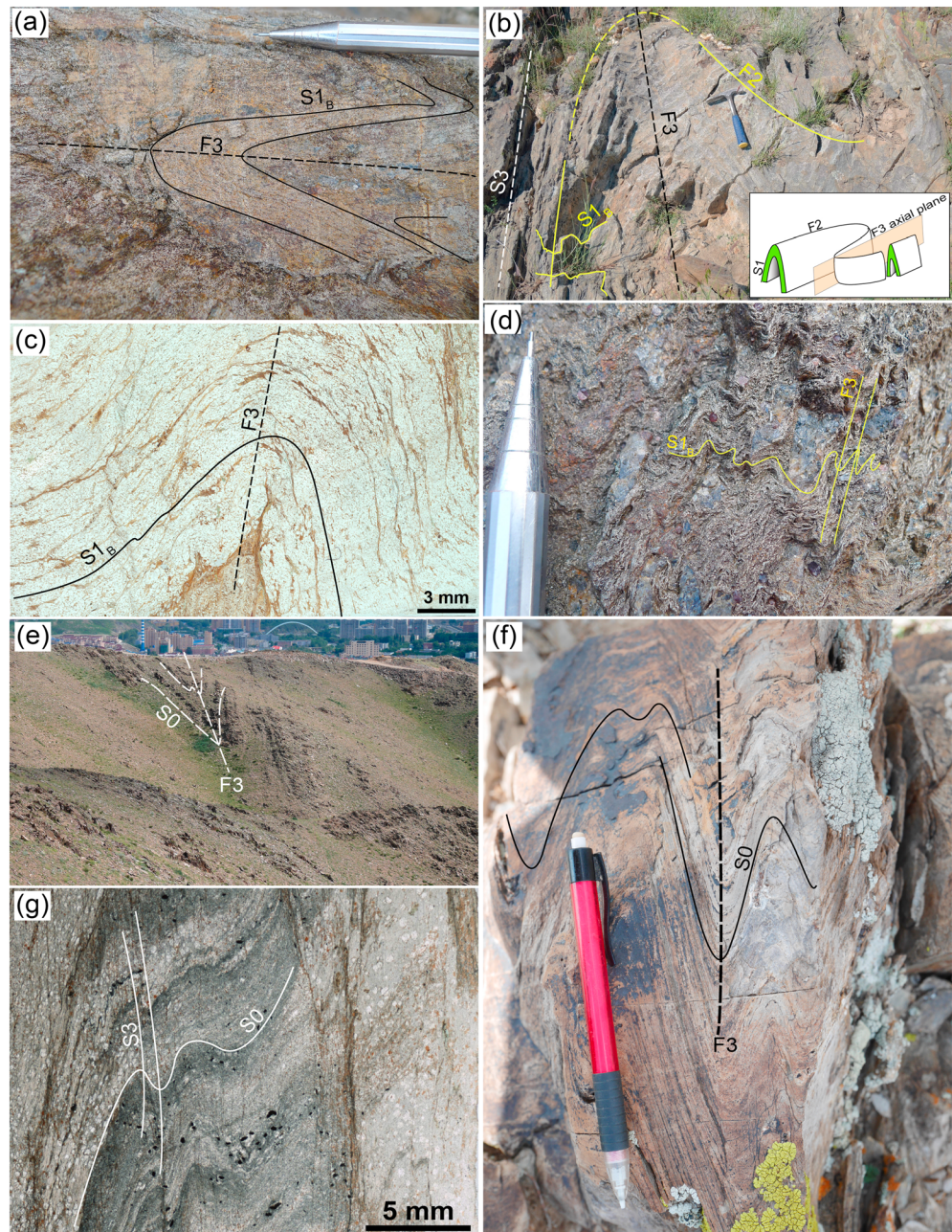
Figure 7. (a–d) Macroscopic and microscopic structures of the metamorphosed Habahe Group rocks: (a) subvertical Barrovian-type $S1_B$ fabric folded by F3 upright folds. (b) Barrovian-type $S1_B$ fabric folded by F2 upright fold and refolded by upright F3 fold. Note that F2 fold has a subhorizontal hinge. Inset: sketch demonstrating the superposition of F3 on F2 fold. (c) Microscopic structures showing Barrovian-type $S1_B$ fabric folded by F3 fold. (e–g) Macroscopic and microscopic structures show the sedimentary bedding S0 folded by F3 upright folds in the Devonian sedimentary sequence.

Pegmatite dykes that intruded the metamorphosed Habahe Group exhibit different geometry compared to those in the migmatite-magmatite complex. Dykes crosscutting the $S1_B$ metamorphic schistosity of the Habahe Group rocks are tightly folded by the D3 event. In most cases, the pegmatite dykes and lithological layering were brought into approximate parallelism with long limbs of F3 folds (Figures 9b and 9c) where they are strongly flattened and boudinaged within the transposed S3 fabric. In the low strain domains, formed by more competent psammitic rocks, characteristic cleavage refraction in the pegmatite fold limbs can be observed (Figure 9d). However, when the pegmatite dykes intruded more competent migmatite-
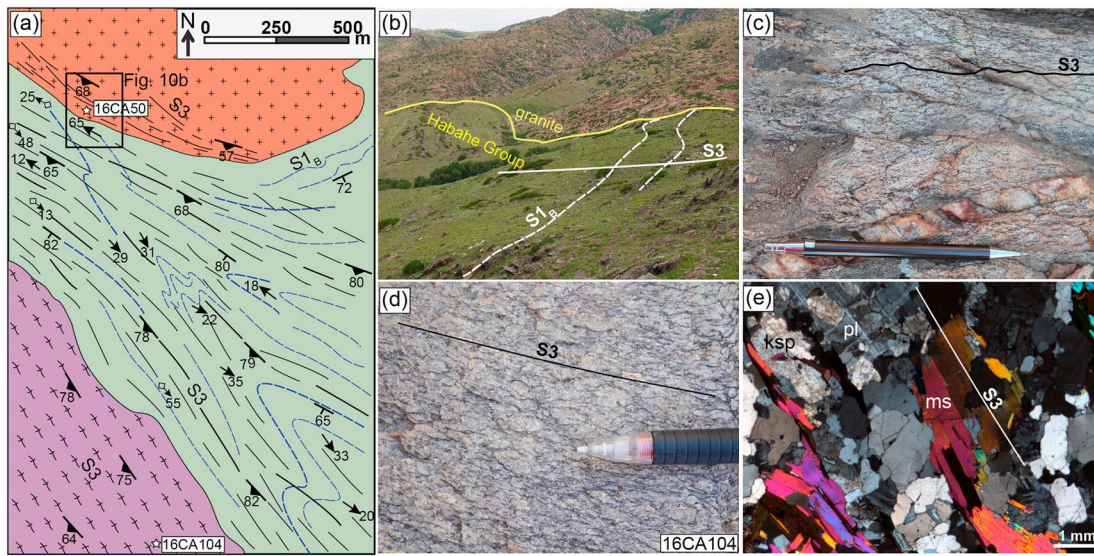
Figure 8. (a) Geological map shows gneissic garnet-bearing granite crosscutting $S1_B$ fabric in the Habahe Group schists (NW corner) and late muscovite granite elongated parallel with the regional S3 foliation (SW corner). Locations of zircon U-Pb geochronological samples are indicated. For legend see Figure 3. (b) Garnet-bearing granite crosscutting metamorphic $S1_B$ fabric in the surrounding Habahe Group schists. (c) Subsolidus deformation of granite forming mylonitic S3 foliation along the contact with the Habahe Group schists. (d) Muscovite granite shows a magmatic foliation parallel to S3. (e) Photomicrograph of the muscovite granite showing the magmatic foliation marked by preferred alignment of euhedral crystals of muscovite (ms), plagioclase (pl), and K-feldspars (ksp). Note weakly to undeformed quartz grains.

magmatite complex, they were only gently folded into open F3 folds (Figure 9e). The pegmatite dykes are even perpendicular and almost unfolded to the NW-SE striking S3 foliation in a zone of strong D3 deformation along the contact between the migmatite-magmatite complex and the metasedimentary rocks (Figures 9a and 9b, samples 15CA31 and 16CA101). The orientation of pegmatites dykes perpendicular to the XY plane of the D3 strain ellipsoid (S3 cleavage) indicates that they were emplaced as tensional gashes parallel to principal compressive stress (Mode I fractures). Intense folding of the pegmatite dykes crosscutting incompetent schists of the metamorphosed Habahe Group further indicates that they were emplaced during the D3 event.

Apart from pegmatite dykes, a tabular body of muscovite granite elongated parallel with the regional NW-SE trending S3 foliation intruded the Habahe Group mica schists (Figures 2 and 8c, sample 16CA104). This granite is characterized by a strong magmatic foliation, marked by the preferred alignment of euhedral muscovite, plagioclase, and K-feldspar phenocrysts without any plastic deformation and/or recrystallization (Figures 8d and 8e). These features are indicative of free rotation of crystals without significant interference with neighboring minerals in viscously flowing magma (Paterson et al., 1989). The magmatic foliation strikes NW-SE, in continuity with the external regional schistosity S3 (Figure 8a). All these structural features point to a syntectonic emplacement of the granite body during the D3 event.

4. Deformation-Metamorphism Relationships and Pressure-Temperature Evolution

In the studied area, the metamorphic grade is generally low in the Devonian sedimentary succession, medium in the Habahe Group metasedimentary rocks, and high in the migmatite-magmatite complex. The main schistosity in the Devonian rocks is developed up to the biotite zone conditions. The metamorphosed Habahe Group rocks are characterized by a succession of Barrovian-type garnet, staurolite, kyanite, sillimanite isograds, and the migmatite layering of the migmatite-magmatite complex coincides with the garnet-cordierite zone. In addition, the andalusite is present in discontinuous domains that are in some places overlapping the staurolite, kyanite, and sillimanite zones (Figure 10). The crystallization-deformation relationships are used here to correlate the growth of index metamorphic minerals with the individual successive macroscopic fabrics. From these microstructural relations, a qualitative Pressure-Temperature (P-T) path segment for each metamorphic fabric is deduced for individual metamorphic zones.
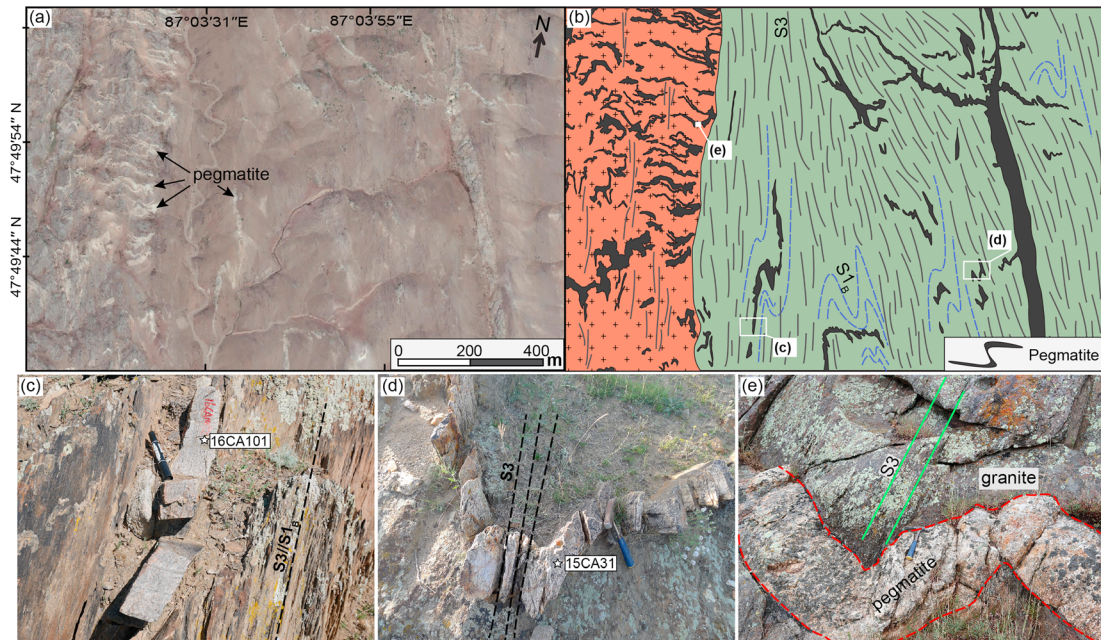
Figure 9. (a) Aerial photograph and (b) redrawn lithological map of the region showing trajectories of S1 and S3 and deformational patterns of pegmatites. For legend see Figure 3. (c) A pegmatite vein crosscuts the $S1_B$ metamorphic foliation of the metamorphosed Habahe Group, both structural elements were brought into approximate parallelism with F3 limbs during folding (position of geochronology sample is indicated). (d) A pegmatite vein crosscutting the $S1_B$ metamorphic foliation in the metamorphosed Habahe Group, both are folded during the D3 event (position of geochronology sample is indicated). (e) Pegmatite dyke intruding the granite of the migmatite-magmatite complex and gently folded by F3.

Field observations suggest that mineral isograds of garnet, staurolite, kyanite, and sillimanite are broadly parallel to the S1 fabric and refolded by the regional D3 folding (Figure 10). Microstructural observations suggest that garnet, staurolite, kyanite, and sillimanite grew parallel to the S1 fabric (Figures 11a–11d). Straight inclusions trails of quartz, biotite and ilmenite in the garnet, staurolite, and kyanite porphyroblasts are continuous with the external $S1_B$ fabric, attesting to the syn-D1 growth of these porphyroblasts. The garnet-cordierite zone in the migmatite-magmatite complex is characterized by stromatic to nebulitic $S1$-2_M foliation that is defined by quartz-feldspar $\pm$ cordierite-bearing leucosome bands associated with garnet-sillimanite-biotite $\pm$ cordierite-bearing melanosome layers (Figure 11e). It is also evident that the staurolite-, kyanite-, and sillimanite-bearing fabrics are heterogeneously overprinted by randomly oriented andalusite porphyroblasts (Figures 11f–11i). As a result, crenulated $S1_B$ fabric and relics of almost all former S1 index minerals can be locally observed inside andalusite porphyroblasts (Figures 11f–11h). Some andalusite grains are even oriented parallel with the axial cleavage of F3 folds (Figure 11i), suggesting syn-D3 growth. A narrow sillimanite zone is parallel to the regional S3 foliation along the contact with the migmatite-magmatite complex (Figure 3). Such sillimanite-bearing fabric could represent either the rotated S1 foliation in the limb of an F3 fold or a new S3 foliation that transposed all previous structures during the Permian, as proposed by Wang et al. (2014).

A simplified schematic P-T diagram is used in order to quantify P-T evolution of the medium-grade metamorphosed Habahe Group and the high-grade migmatite-magmatite complex (Figure 11j). Schematic stability of garnet, staurolite, kyanite, sillimanite, and andalusite in the subsolidus conditions and stability of K-feldspar, muscovite, and cordierite in the suprasolidus conditions are retrieved from previous studies in the Chinese and Mongolian Altai (Burenjargal et al., 2014; Jiang et al., 2015;
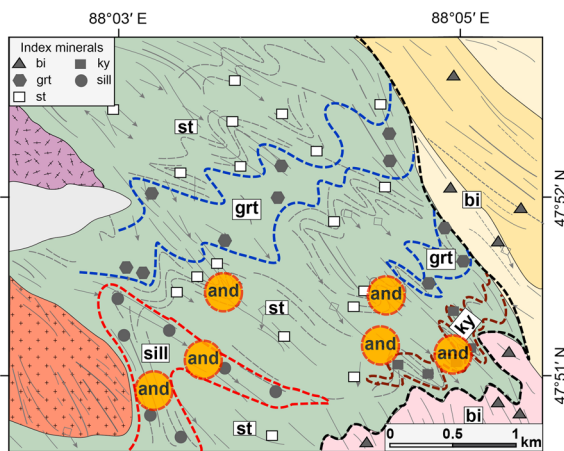

Figure 10. Map showing the occurrences of metamorphic minerals and the associated isograds in the studied area. Mineral abbreviations used are as follows: bi = biotite; grt = garnet; st = staurolite; ky = kyanite; sill = sillimanite; and = andalusite. See Figure 2 for location.
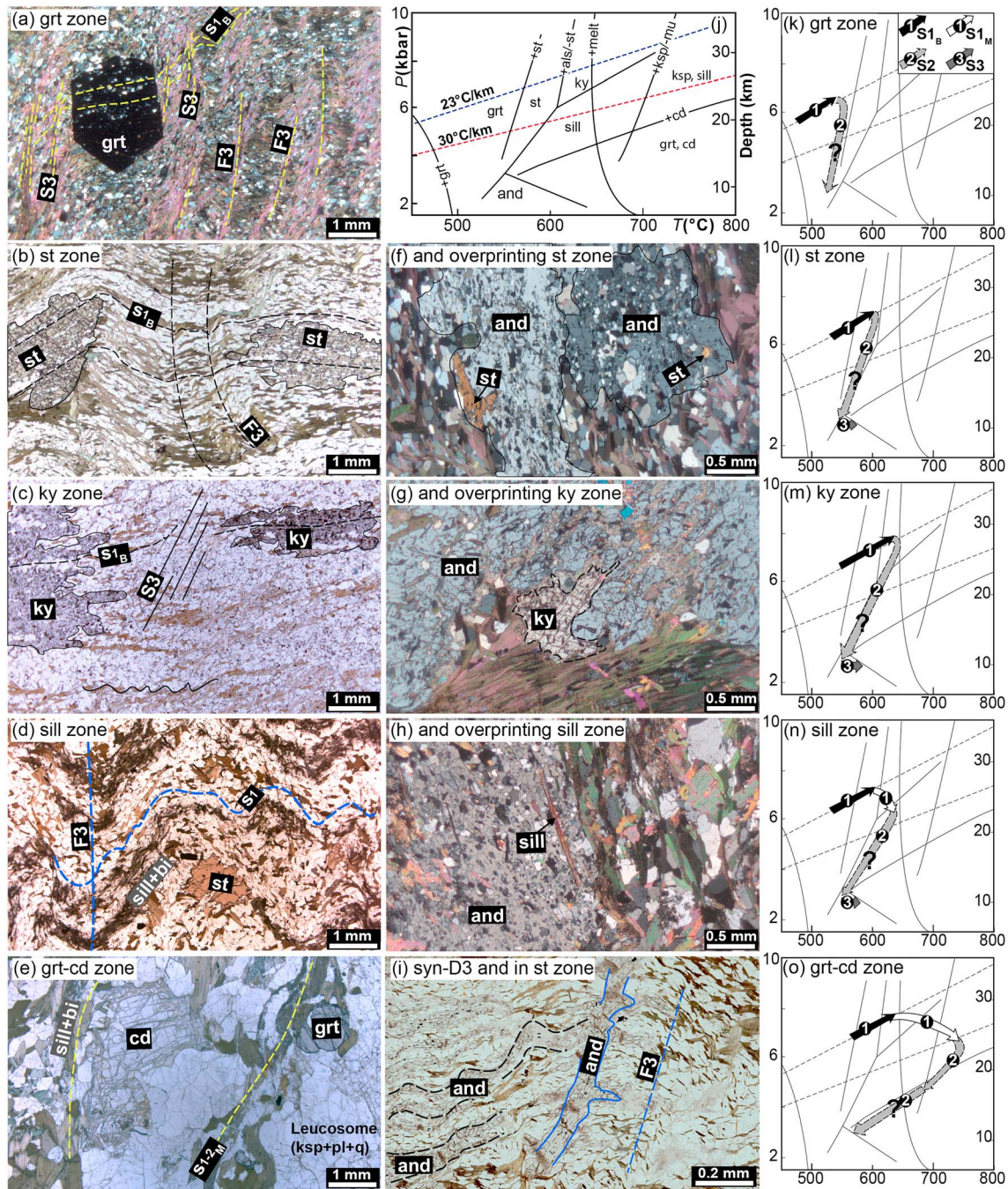
Figure 11. Photomicrographs illustrating the relationships between structures and metamorphic minerals for the representative metamorphic zones in the studied area. (a–c) Garnet, staurolite, and kyanite have $S1_B$ mineral inclusion trails, indicating syn-D1 growth. $S1_B$ fabrics were further reworked by F3 folds. (d) Sillimanite parallel to the S1 foliation affected by F3 microfolds. Note some preserved staurolite fragments, probably the relics of former fabrics, suggesting sillimanite zone experienced staurolite-stability field. (e) Aligned biotite and sillimanite interlayered with leucosomes consisting of ksp + pl + q ± cd define the $S1\text{-}2_M$ in the nebulitic migmatite. (f–h) Andalusite porphyroblasts overgrowing the S1 index minerals staurolite, kyanite, and sillimanite. (i) Andalusite includes the crenulated $S1_B$ fabric and grew parallel with the axial cleavage of F3 folds indicating its growth during D3. (j) Schematic mineral stability fields drawn using pseudosections of Wei et al. (2007) and Jiang et al. (2015). (k–o) Qualitative P-T paths deduced from the crystallization of the mineral succession in the garnet, staurolite, kyanite, sillimanite, and garnet-cordierite zone, respectively. Note that inferred P-T paths of S2 are labeled with a question mark, since fabric transposition associated with D2 deformation was observed for these rocks. The solidus is modified from Ebadi and Johannes (1991). Additional mineral abbreviations: als = aluminosilicate polymorphs; cd = cordierite; ksp = K-feldspar; pl = plagioclase; q = quartz.

Wei et al., 2007). The wet granite solidus is after Ebadi and Johannes (1991). Two geotherms of 23 and 30 °C/km, regarded as typical for the Barrovian and migmatite domains in the Altai (Jiang et al., 2015; Jiang et al., 2016; Wei et al., 2007), are also shown.

In the metamorphosed Habahe Group, growth of garnet, staurolite, and kyanite in the $S1_B$ foliation implies that prograde metamorphism is syntectonic with the $D1_B$. A prograde P-T path starting from the garnet-stability field, evolving along the geotherm of 23 °C/km, and reaching the peak in the related garnet-, staurolite-, and kyanite-stability fields can be retrieved for each of these $S1_B$ (Figures 11k–11m). This is consistent with the results of Wei et al. (2007), who reported prograde garnet growth from 510/6.1 to 580 °C/6.8 kbar for garnet zone, from 560/6–7 to 598 °C/7.8 kbar for staurolite zone, and from 570/7.7 to 630 °C/8.7 kbar for kyanite zone in this region. Inferring the prograde P-T path for the sillimanite zone is not straightforward. The presence of staurolite relics in the S1 foliation suggests that the prograde P-T path initially evolved in the staurolite-stability field before it reached the sillimanite stability. Accordingly, a two-stage evolution can be deduced for the sillimanite zone, that is, an early stage evolving along the Barrovian metamorphic gradient in the garnet-staurolite stability ($S1_B$ in Figure 11n) and a late stage from the staurolite to the sillimanite stability field ($S1_M$ in Figure 11n), probably contemporaneous with the $S1_M$ in the migmatite as discussed in the next section. This view is also supported by the pseudosection modeling of Wei et al. (2007) who suggested a prograde P-T path from 580/7.5 to 650 °C/8 kbar at an early stage in the staurolite-kyanite stability, followed by a later re-equilibration at 680 °C/6.7 kbar in the sillimanite stability field, implying an increase of temperature and a decrease of pressure. The presence of andalusite porphyroblasts overprinting preexisting staurolite-, kyanite-, and sillimanite-bearing assemblages indicates a decompression P-T path into the andalusite stability for each of these metamorphic zones (Figures 11k–11n; see also Wei et al., 2007).

The mineral assemblage defining $S1-2_M$ in the migmatite complex indicates that the migmatite once equilibrated in the garnet-cordierite-sillimanite-K-feldspar stability field (Figure 11o). The observed mineral assemblage in the migmatites is typical of equilibration close to the solidus during cooling (e.g., Štípská et al., 2008; White et al., 2004), and a cooling P-T path can be therefore traced from higher P-T conditions to the solidus. In the current case, a cooling P-T path can be traced starting at least through the garnet-sillimanite-K-feldspar stability field, since such assemblage occurs in the $S1-2_M$ foliation. This is in accordance with the studies of Wei et al. (2007) and Jiang et al. (2015), who proposed cooling evolving from the garnet-sillimanite-K-feldspar stability field (800 °C/7 kbar) to the garnet-cordierite stability field (680–710 °C/5.5–6 kbar) for nearby, compositionally similar migmatite massifs. Inclusions of staurolite and kyanite preserved in the zoned garnet were occasionally observed in the nearby migmatite (garnet-cordierite zone), which is compatible with a prograde P-T path evolving from the staurolite-stability field to the kyanite-stability field as suggested by Jiang et al. (2015). However, for the studied migmatite, no such preexisting fabrics and/or assemblages that could be directly correlated with the prograde P-T path have yet been observed. A similar prograde P-T path ($S1_B$ in Figure 11o) is assigned for the studied migmatite on the basis of the work of Jiang et al. (2015). In other words, we infer a prograde P-T path associated with the transition from the subsolidus staurolite-kyanite stability to the suprasolidus garnet-sillimanite-K-feldspar stability related to the development of the $S1_M$ foliation in the migmatite (Figure 11o).

The P-T data summarized above suggest that the garnet-cordierite grade migmatite-magmatite complex possibly evolved from a depth about 30 km or more, while the dominant garnet and staurolite zones of the metamorphosed Habahe Group recorded depths of 20–30 km. The Devonian metasedimentary succession, reaching the biotite zone conditions, probably evolved in shallower depths compared to the metamorphosed Habahe Group. This is in agreement with Jiang et al. (2016) and Broussolle et al. (2018), who suggested that the Chinese Altai crust can be considered as vertically layered edifice represented by (1) molten or even granulitized Ordovician Habahe Group forming the orogenic lower crust, (2) greenschist- to amphibolite-facies Habahe Group intruded by Devonian granitoids forming the orogenic middle crust, and (3) Devonian volcanoclastic succession with surface volcanism representing the orogenic upper crust. Such definition is not correlated with the geophysical definition of mafic lower, intermediate middle, and felsic upper crust (Christensen & Mooney, 1995) but is based on the position of rocks within the orogen (e.g., Schulman et al., 2005). Accordingly, the studied migmatite-magmatite complex, the metamorphosed Habahe Group,

and the Devonian metasedimentary succession can be considered as typical Chinese Altai orogenic lower, middle, and upper crustal levels, respectively.

5. Geochronology: U-Pb Zircon and Monazite

5.1. Sampling Strategy

Structural analysis and restorations enable us to understand the sequence of deformational fabrics and the spatial relations between the migmatite-magmatite complex, the Ordovician Habahe Group metasedimentary rocks, and its overlying Devonian sedimentary succession. In order to provide critical geochronological constraints on the individual fabrics, samples from the key lithological units were collected for zircon and monazite U-Pb dating.

Six samples were collected for zircon dating. One sample was collected from a leucosome-bearing two-mica granite (sample 15CA24; Figures 2b and 5b) of the migmatite-magmatite complex, and another sample was collected from a garnet-bearing granite (sample 16CA50; Figures 2b and 8a) that intruded the metamorphic Habahe Group and crosscuts the $S1_B$ in the latter. One metarhyolite (15CA27; Figures 2 and 3) was collected from the low-grade Devonian metavolcanic sequence. Three samples were collected from late magmatic bodies, including one undeformed muscovite granite (sample 16CA104; Figures 2b and 8a) and two pegmatites (samples 15CA31 and 16CA101; Figures 2b, 9c, and 9d). The two pegmatite samples (samples 15CA31 and 16CA101) were also selected for monazite separation.

5.2. Analytical Methods

Zircon and monazite grains were extracted using standard heavy liquid and magnetic techniques and then purified by hand picking under a binocular microscope. These grains were then mounted in epoxy resin and polished. The internal zircon structures were documented by imaging using an electron microprobe (JXA-8100, JEOL) equipped with a Mono CL3 cathodoluminescence (CL) system at the Guangzhou Institute of Geochemistry, Chinese Academy of Sciences. Monazite grains were imaged with backscattered electrons and secondary electrons using the same microprobe instrument.

Zircon samples 15CA24 and 16CA50 were analyzed by a pulsed Resonetic 193-nm ArF excimer laser ablation system coupled with an Agilent 7500a ICP-MS at the GIG-CAS, following the analytical procedure described by Li et al. (2012). Most analyses were performed with a beam diameter of 30 μm. Temora zircon standards (416.75 Ma; Black et al., 2003) were used for calibration. The mass fractionation correction and isotopic results for the analyses were calculated by ICPMSDataCal (version 7.0; Liu et al., 2008). Zircons from samples 15CA27, 15CA31, 16CA101, and 16CA104 were analyzed by a CamecaIMS-1280 ion microprobe established at GIG-CAS, following the analytical procedure similar to Li et al. (2009). The primary ion beam with an intensity of ~10 nA was accelerated at −13 kV. The ellipsoidal spot is about 20 μm × 30 μm in size. Calibration of Pb/U ratios is relative to the standard zircon Plesovice (337.13 Ma; Sláma et al., 2008). Measured compositions were corrected for common Pb using nonradiogenic [204]Pb, assuming that for low counts of [204]Pb, common Pb is mainly surface related (Ireland & Williams, 2003) and has a composition of present-day average crustal composition (Stacey & Kramers, 1975). The data reduction was carried out using the in-house designed geochronology software of Dr. Martin Whitehouse. U-Pb dating of monazite samples 15CA31 and 16CA101 was performed using a GeolasPro laser ablation system coupled with an Agilent 7700e ICP-MS instrument at China University of Geoscience (Wuhan). Helium was used as the carrier gas, and argon was used as the makeup gas which mixed with the carrier gas via a T-connector before entering the ICP. A "wire" signal smoothing device is included in this laser ablation system, by which smooth signals are produced even at very low laser repetition rates down to 1 Hz which is suitable for in situ U-Pb dating of high-U minerals (Hu et al., 2015). In this work, the spot size and frequency of the laser were set to 10 μm and 3 Hz, respectively. Monazite standard 44069 (ca. 425 Ma; Aleinikoff et al., 2006) was used as an external standard. Each analysis incorporated a background acquisition of approximately 20–30 s followed by 50 s of data acquisition from the sample. The mass fractionation correction and isotopic results were calculated by ICPMSDataCal as well. For both zircon and monazite U-Pb dating, uncertainties on single analyses are reported at the 1σ level; mean ages for pooled U-Pb analyses are quoted with a 95% confidence interval, and these data are presented in Table S1 in the supporting information. The age calculations and concordia plots for all methods were done using ISOPLOT (version 3.0; Ludwig, 2003).
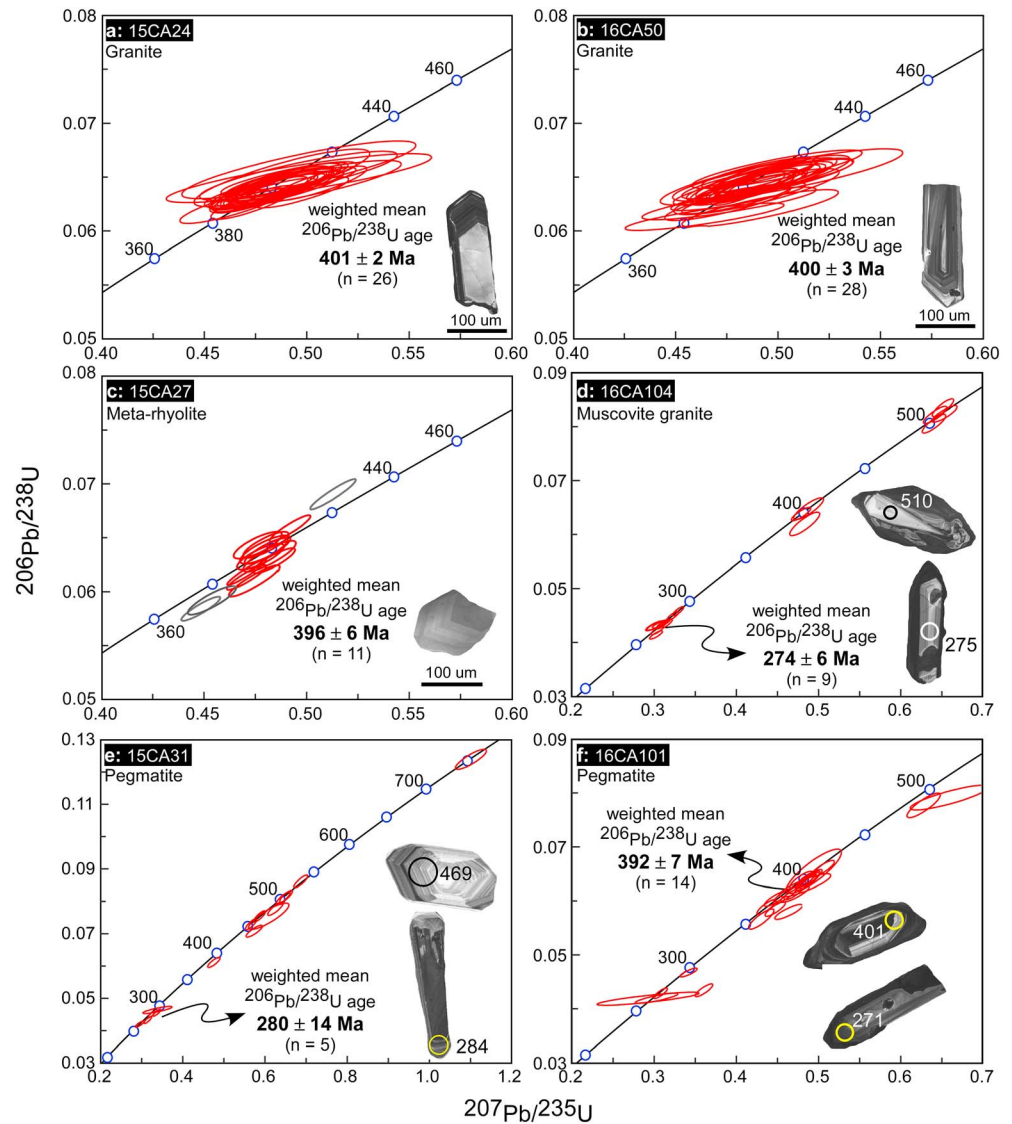
Figure 12. U-Pb concordia diagrams for zircons from the migmatite-magmatite complex (a) and (b), the metavolcanic rock of the Devonian succession (c), late muscovite granite (d), and pegmatites (e) and (f). See Figure 3 for location. Note that less concordant points shown in gray circles in (b) and (c) were excluded from weighted mean age calculation.

The error correlation of $^{206}Pb/^{238}U$–$^{207}Pb/^{235}U$ used in the Concordia and Tera-Wasserburg plots is between 0.85 and 0.95, a value from a long-term statistics of the laboratory.

5.3. Results

5.3.1. Devonian Magmatism

Zircons from two-mica granite sample 15CA24 and garnet-bearing granite sample 16CA50 exhibit similar morphological and internal structures, irrespective of dissimilar mineral assemblages of their host rocks. Zircons from both samples are predominantly euhedral and prismatic, with a minor subhedral population with slightly rounded terminations. Most of the zircon grains exhibit clear igneous-related oscillatory zoning without inherited cores in the CL images (Figures 12a and 12b). LA-ICPMS analyses of samples 15CA24 and 16CA50 yielded concordant Middle Devonian ages and defined simple and tight age populations with weighted mean $^{206}Pb/^{238}U$ ages of 401 ± 2 Ma (MSWD = 0.36) and 399 ± 3 Ma (MSWD = 1.15), respectively (Figures 12a and 12b).
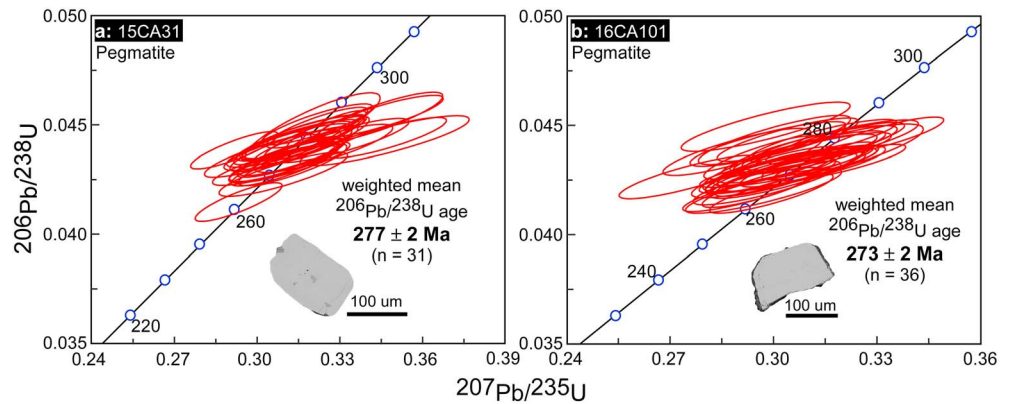
Figure 13. (a, b) U-Pb concordia diagrams for monazites from pegmatite veins.

Zircons from metarhyolite sample 15CA27 are euhedral and stubby and generally display simple oscillatory zoning in CL images (Figure 12c). Among the 14 grains analyzed by SIMS, 11 analyses yielded concordant ages clustering around 400 Ma and the three remaining analyses gave less concordant ages, likely affected by Pb loss due to later thermal perturbation. The 11 concordant analyses were used to determine a weighted mean $^{206}Pb/^{238}U$ age of 396 ± 6 Ma (MSWD = 1.15). Accordingly, these three samples document a prominent Middle Devonian magmatism in the region.

5.3.2. Early Permian Magmatism

Zircons from the muscovite granite (sample 16CA104) and the two other pegmatite samples (15CA31 and 15CA101) have very similar size and shape, as well as internal patterns. Broadly, zircons from these samples can be divided into two types. The first type consists of euhedral long-prismatic crystal with a length/width ratio >4:1 (Figures 12d–12f). These grains generally display concentric oscillatory zoning; however, many of the original zoning are partly replaced by low luminescence rims. The second type is characterized by euhedral-subhedral stubby-prismatic crystal shapes with length/width ratios up to 3:1. Some of them have corroded or rounded terminations. In this zircon type, some grains show magmatic oscillatory zoning whereas others display complicated internal structures (Figures 12d–12f). Analyses of either the cores or the low luminescence rims of the first type of zircons yielded similar individual $^{206}Pb/^{238}U$ ages varying between 295 and 261 Ma. Analyses of this type of zircon form clusters corresponding to weighted mean ages of 274 ± 6 Ma (MSWD = 3.7, 16CA104) and 280 ± 14 Ma (MSWD = 6.9, 15CA31), which are interpreted as the crystallization ages of the muscovite granite and pegmatites (Figures 12d and 12e). Analyses of the second zircon type gave older ages with peaks at ca. 400 and 500 Ma, resembling the main zircon populations of the adjacent Devonian granites and the Habahe Group, respectively (Jiang et al., 2011). These grains are interpreted as xenocrysts that were possibly inherited from the surrounding rocks or from the magma source.

Pegmatite samples 15CA31 and 15CA104 were selected for further U-Pb monazite dating. Monazite grains from both samples show comparable features and are mostly 250- to 300-µm unzoned subhedral to euhedral (Figure 13). The 31 and 36 analyses of samples 15CA31 and 15CA104 form tight clusters on the concordia diagrams with weighted mean $^{206}Pb/^{238}U$ ages of 277 ± 2 Ma (MSWD = 1.6) and 273 ± 2 Ma (MSWD = 1.4), respectively (Figure 13). These ages are consistent with the youngest zircon U-Pb ages of the samples within analytical uncertainties, confirming that the pegmatites are Early Permian.

6. Discussion

6.1. Structural Evolution of Individual Deformational Episodes

Our field observations have demonstrated that the studied area experienced two significant folding events, during which the attitude of previously horizontal orogenic fabric was extensively modified. Accordingly, we first discuss the origin of the S1 horizontal fabric, followed by a discussion on the structural evolution of the two, D2 and D3, folding events.

6.1.1. Origin of S1 Horizontal Fabric

The study area is characterized by a ubiquitous subhorizontal magmatic/migmatitic ($S1_M$) foliation and Barrovian metamorphic foliation ($S1_B$) in the migmatite-magmatite complex (i.e., the orogenic lower crust) and in the amphibolite-facies Ordovician Habahe Group rocks (i.e., the orogenic middle crust), respectively. The $S1_M$ banding and extensional melt-bearing shear bands indicate melt-assisted horizontal extension associated with vertical shortening of weak horizontal multilayer system (Cosgrove, 1997) at the orogenic lower crust. On the other hand, the horizontal foliation $S1_B$ in the orogenic middle crust is contemporaneous with crustal shortening and thickening rather than extension and thinning. This difference raises the question as to whether the thinning of the orogenic lower crust and thickening of the orogenic middle crust were coeval during inverse ductile thinning, as exemplified by Jeřábek et al. (2012), or represent two distinct phases of orogenic evolution.

This problem is impossible to be solved by the means of structural geology only, since the studied $S1_B$ and $S1_M$ fabrics seem to be parallel and shared the same D2 and D3 deformation overprints. However, the available geochronological, crystallization-deformation relationships and P-T data described above can potentially provide critical constraints. The granite sample (15CA24), collected from the orogenic lower crust, has a strong extensional subhorizontal magmatic $S1_M$ fabrics. This granite yielded a zircon U-Pb age of ca. 401 Ma, probably dating the extensional event. On the other hand, the other garnet-bearing granite (sample 16CA50) intruded and crosscuts the Barrovian-type mineral isograds in the orogenic middle crust. This granite gave a zircon U-Pb age of ca. 400 Ma, clearly postdating the formation of the $S1_B$ fabrics. These ages imply that the extensional $S1_M$ fabric postdates the Barrovian $S1_B$ fabrics.

In addition, relics of typical Barrovian-facies $S1_B$ minerals (staurolite and kyanite) are preserved in the melt-present garnet-sillimanite-cordierite-K-feldspar-bearing horizontal foliation $S1_M$ (Jiang et al., 2015). Previous thermodynamic modeling has suggested a prograde P-T path associated with the relict staurolite-kyanite assemblage along a typical Barrovian-facies metamorphic field gradient followed by evolution at much higher temperature at suprasolidus conditions (Jiang et al., 2015). These findings imply two-stage metamorphic history where the rocks were buried during crustal thickening as recorded by the Barrovian metamorphism and subsequently melting and horizontally stretching in the orogenic lower crust. Similarly, P-T evolution of the sillimanite zone also suggests a P-T evolution from a typical Barrovian-type burial metamorphism to a significantly higher geothermal gradient (Figure 11n; see also Wei et al., 2007). It is can be therefore concluded that the orogenic lower crust probably shared the early Barrovian-type $S1_B$ fabric with the orogenic middle crust at an early phase of crustal thickening ($D1_B$) and that such fabric was completely erased and replaced by the parallel and hotter $S1_M$ foliation during a later extensional and moderate crustal thinning phase ($D1_M$).

6.1.2. Upright D2 Folding: Result of NW-SE Horizontal Shortening

Field observations and geometrical structural analysis showed that the horizontal fabrics $S1_M$, $S1_B$ and sedimentary bedding S0 were reworked by upright F2 folding. In the orogenic lower crust, the D2 folding resulted in transposition of early fabrics and formation of composite $S1\text{-}2_M$ foliation, still under the presence of melt. In the orogenic middle crust, signs of structural transposition are lacking in the field; however, the locally preserved upright F2 folds with subhorizontal hinges together with the generally opposite plunge of the F3 fold axes attest to the widespread existence of the F2 folding. In the orogenic upper crust, the bedding S0 was also rotated to upright or moderately dipping position before D3 folding. The variable expressions of the D2 upright folding in the three crustal levels can be also inferred from the distributions of the F3 axes maxima in the stereonets. The large distance between the F3 axes maxima and the center of the stereonet in the orogenic lower crust suggests the existence of moderate to open interlimb angle of F2 folds. In the orogenic middle crust, close to tight interlimb angle of F2 folds can be deduced from the single subvertical maximum of the F3 fold axes. Likewise, moderate to close interlimb angle of F2 folds in the orogenic upper crust could be inferred. The F2 fold shape variations with depth may indicate that the degree of the D2 shortening decreases from the deeper and rheologically weak orogenic lower crust to shallower middle and upper crustal levels. The structural restoration of F2 folds with NE-SW plunging subhorizontal hinges and NW or SE dipping moderately to steeply dipping limbs suggest that the F2 upright folding was associated with ~NW-SE directed shortening.
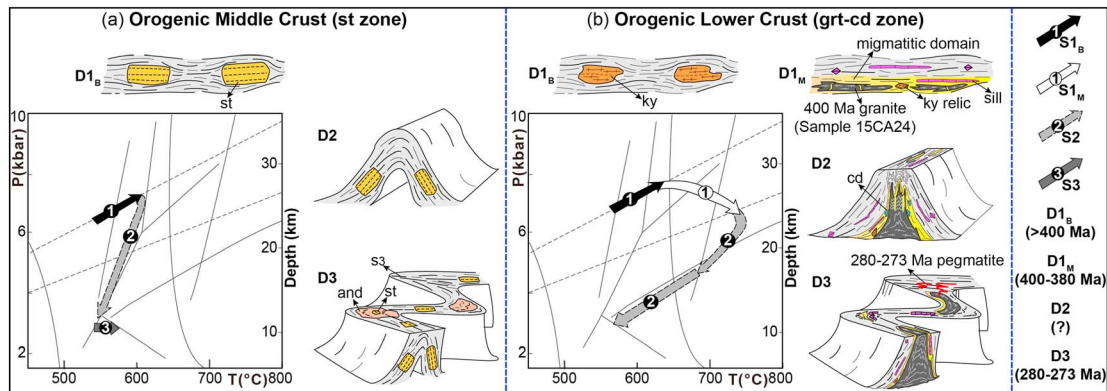
Figure 14. Schematic P-T-t-D evolution of the orogenic (a) middle and (b) lower crust, in terms of the staurolite and garnet-cordierite zones, respectively. Schematic mineral stability fields correspond to those in Figure 11j. Interpretative sketches (not to scale) show macrostructure and/or microstructures associated with deformation episodes. See text for details.

6.1.3. D3 Upright Folding and Emplacement of Pegmatite Dykes: Result of NE-SW Shortening

This study demonstrates that D3 deformation reflects significant NE-SW directed shortening of all crustal levels. It is associated with crustal-scale formation of the upright F3 folds and steep NW-SE trending cleavage fronts, which reworked heterogeneously but intensely all the previous fabrics and structures. The shortening is also related to important magmatic activity characterized by emplacement of pegmatite dykes along large tensional gashes orthogonal to S3, followed by their folding into tight F3 folds in the weak Habahe Group metasedimentary rocks.

6.2. Pressure-Temperature-Time-Deformation Evolution

In this section, newly obtained structural and geochronological constraints are combined with metamorphic and zircon U-Pb data sets in order to establish the Pressure-Temperature-Time-Deformation (P-T-t-D) evolution of the region. A sketch diagram displaying the deformation and P-T evolution of the staurolite and garnet-cordierite zones related to early $S1_B$ and $S1_M$ fabrics during late D2 and D3 events in the orogenic lower and middle crust is given in Figure 14.

6.2.1. P-T-t-D1 Evolution

It has been shown above that $S1_B$ developed in the garnet, staurolite, and kyanite zones during prograde P-T evolution. Previous pseudosection modeling of Wei et al. (2007) defined typical Barrovian-type metamorphic field gradients of 21–26 °C/km for these metamorphic zones. The finding of staurolite and kyanite relics in the prograde garnet from the garnet-cordierite zone has also been interpreted as an indication of the Barrovian-facies metamorphic evolution (Jiang et al., 2015). These features indicate that both the orogenic lower and middle crust of the study area were affected by a progressive burial during the course of $D1_B$, leading to the development of metamorphic isograds up to staurolite and kyanite zone for the orogenic middle and lower crust, respectively (Figures 14 and 15a). This corresponds to a maximum burial to depth of >30 km in the orogenic lower crust (Jiang et al., 2016; Wei et al., 2007). The timing of this burial history is currently undetermined, but it should predate the 400-Ma granite (sample 16CA50) that crosscuts the $S1_B$ foliations in the orogenic middle crust (Figure 15a).

The $S1_B$ fabric in the orogenic lower crust was reworked by geometrically parallel $S1_M$ foliation in the garnet-cordierite and sillimanite zones, resulting in reequilibration of the metamorphic paragenesis at higher temperatures (Figures 11n, 11o, and 14b). The inferred P-T paths indicate that the formation of the horizontal extensional $S1_M$ fabrics in the migmatite-magmatite complex is kinematically linked to either isobaric heating or heating associated with moderate pressure decrease (Figure 14b). The timing of the transition from burial to extension can be constrained by the ca. 400-Ma zircon U-Pb ages of granites with $S1_M$ melt-bearing shear bands in the migmatite-magmatite complex (sample 15CA24; Figure 14b) and by the horizontally layered felsic volcanic rock (sample 15CA27) extruded in the orogenic upper crust (Figure 15a). All these new ages corroborate the timing of Devonian regional anatexis determined by U-Pb dating of metamorphic zircon rims in migmatitic paragneisses (ca. 390 Ma; Jiang
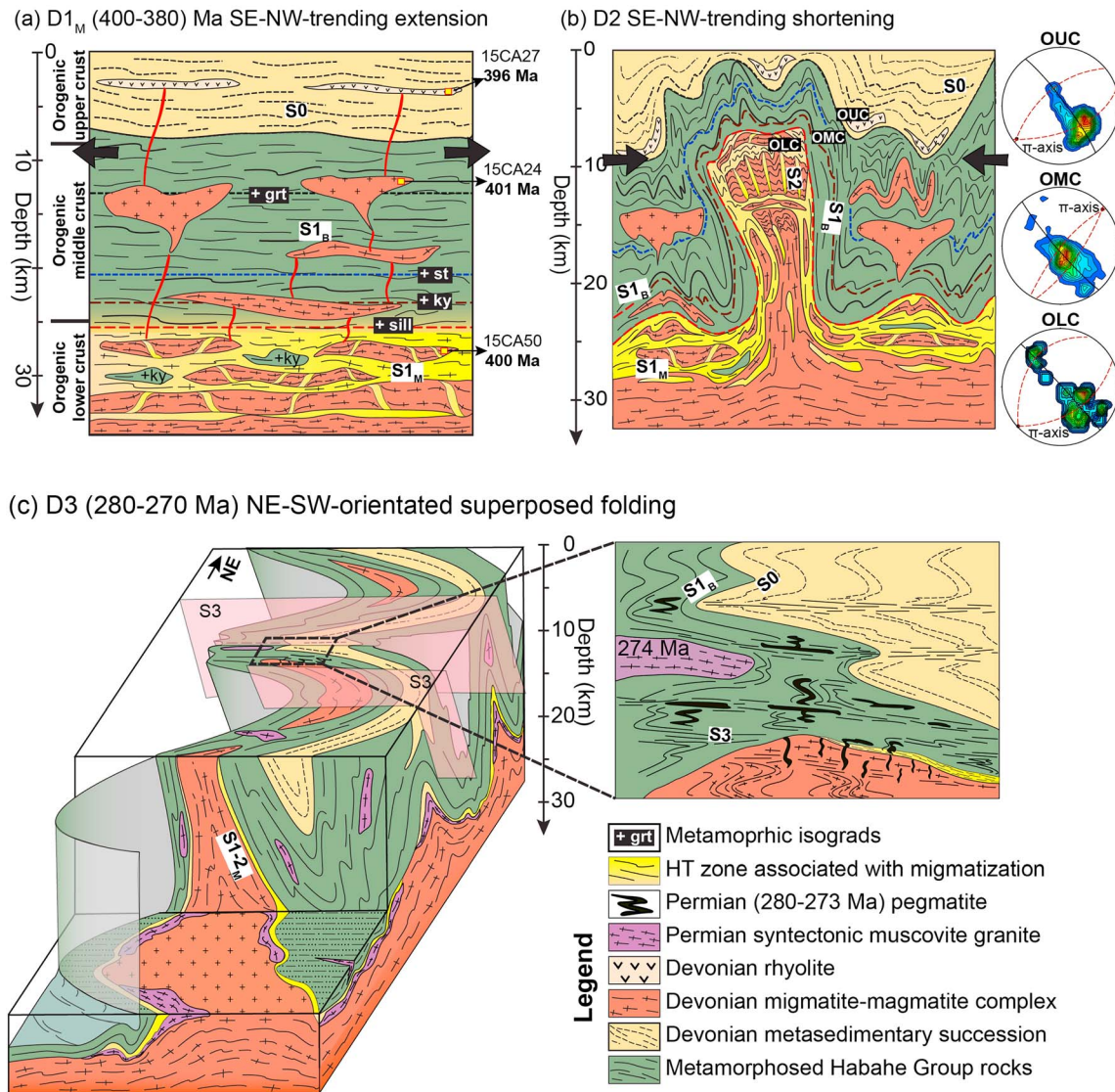
Figure 15. Interpretative evolutionary tectonic model. (a) Reworking of Barrovian-type S1$_B$ fabric and formation of horizontal S1$_M$ fabric associated with anatexis in deep crustal levels and supracrustal deposition of Devonian sedimentary sequence during the D1$_M$ extension. Idealized location of studied geochronological samples and positions of metamorphic isograds are shown. (b) Upright F2 folding associated with extrusion of partially molten crust from depth and tight to open folding of middle to upper crustal levels. Stereonets of F3 fold axes with indicated perspective positions of prefolding planar structures for the orogenic upper, middle, and lower crust, labeled "OUC," "OMC," and "OLC," respectively. (c) Permian upright folding and emplacement of pegmatite dykes preferentially in tension gashes in response to NE-SW shortening formed the final structures in the study area. Inset shows the different geometries of late pegmatite dykes and granite, which intruded the migmatite-magmatite complex and metamorphosed the Habahe Group (see text for details).

et al., 2010), zircon U-Pb data of horizontal granite sheets, and orthogneisses with melt-bearing shear bands in other parts of the Chinese Altai (ca. 390 to 380 Ma; Broussolle et al., 2018; Zhang et al., 2015). Taken together, all these indicate an important thermal perturbation related to extension and thinning of the orogenic lower crust between 400 and 380 Ma.

6.2.2. P-T-t-D2 Evolution

Next, the significance of the subisothermal decompression P-T paths (Figures 11k–11o) inferred for both orogenic lower and middle crust will be discussed. Associated with this decompression, the S1$_B$ fabrics in different metamorphic zones and hence different crustal levels were exhumed at much shallower levels. The well-preserved peak assemblages, in particular, the S1$_B$ foliation in the orogenic middle crust, suggest that the decompression most likely reflects the exhumation of deep-seated rocks rather than transformation of the older S1$_B$ fabric into a new one. The most likely mechanism is the D2 upright folding, responsible for

verticalization of the subhorizontal metamorphic isograds and juxtaposition of the orogenic lower and middle crust with the orogenic upper crust (Figures 14 and 15b). This scenario is very similar to that of Štípská et al. (2012) who proposed a regional-scale upright folding to explain the juxtaposition of exhumed lower crustal rocks and supracrustal pelitic units in the Bohemian Massif.

The peak assemblages with staurolite, kyanite, and sillimanite were not reequilibrated during exhumation (Figure 14a), probably due to the absence of aqueous fluids that could reverse the prograde reactions (Guiraud et al., 2001; Wei et al., 2007). In contrast, the exhumation of migmatites in the core of antiforms was certainly associated with crystallization of melt and reequilibration, as demonstrated by the presence of leucosomes in the axial planar of F2 folds (Figures 5e, 14b, and 15b). Thus, these axial planar leucosomes can mark the timing of the D2 folding (e.g., Weinberg et al., 2015; Závada et al., 2018). Although we have no specific age constraints for these leucosomes in the current area, we propose that the upright F2 folding follows rapidly the 400- to 380-Ma extension in the deep crust, probably in the early Late Devonian. Magmatism during F2 folding has also been inferred by Jiang et al. (2015) in an area 100 km to the west and by Broussolle et al. (2015) and Lehmann et al. (2017) for the Mongolian Altai. Based on the ingress of magma into the cores of F2 antiforms, the age of F2 folds growth has been estimated to be between 400 and 380 Ma in the Chinese Altai (Jiang et al., 2015) and between 360 and 350 Ma in the Mongolian Altai (Broussolle et al., 2015; Lehmann et al., 2017).

6.2.3. P-T-t-D3 Evolution

The metamorphic history defined by the rocks in the study area ends with the growth of andalusite during D3. This part of evolution was associated with heterogeneous reworking of earlier foliations and partly reequilibration of assemblages of staurolite, kyanite, and sillimanite zones in the andalusite-stability field (Figures 11l–11n). It was shown that this late metamorphic event represents lower pressure conditions and is accompanied by neither burial nor exhumation (Figures 11l–11n) but was related to heating and folding during horizontal shortening (Figures 14a and 15c). The timing of D3 is constrained by intrusion of the 280- to 273-Ma pegmatite dykes (samples 15CA31 and 16CA101) and by emplacement of the syntectonic 274 Ma muscovite granite (sample 16CA104) parallel to S3 cleavage, the axial plane of F3 folds (Figures 14b and 15c). Thus, D3 shortening took place some 100 Ma after D2 exhumation and cooling of the whole edifice, suggesting that the growth of andalusite required additional input of fluids and heat flux that can be correlated with emplacement and crystallization of pegmatites and granites in the study area.

Taken together, the described P-T-t-D paths allow the division of the structural evolution into four main stages affecting variably the studied area: (1) formation of the horizontal Barrovian fabric $S1_B$ in the thickened crust is associated with burial ($D1_B$) before 400 Ma; (2) origin of horizontal migmatite-magmatite fabric $S1_M$ in the orogenic lower crust, nearly erasing the earlier Barrovian-type $S1_B$ fabric, is attributed to an extensional phase ($D1_M$) at 400–380 Ma (Figure 15a); (3) the D2 upright folding, followed soon after extension, is related to exhumation of all high- and medium-grade rocks, causing the juxtaposition of partially molten orogenic lower crust with the low-grade orogenic upper crust and medium-grade orogenic middle crust (Figure 15b); and (4) the D3 upright folding simultaneously with low-pressure/high-temperature metamorphism manifested by growth of syntectonic andalusite and emplacement of 280- to 273-Ma late granite and pegmatite dykes (Figure 15c).

6.3. Implication for Regional Geodynamic Evolution

In the following text, the interpretations discussed above will be integrated with the newly acquired geochronological and structural data from adjacent regions in order to develop large-scale tectonic model of the Altai Orogenic Belt.

6.3.1. Devonian Tectonic Evolution

The Chinese and Mongolian Altai represents a Late Cambrian-Ordovician sedimentary accretionary wedge that formed during more than 50 Ma of retreat of the Palaeo-Pacific subduction system (Jiang et al., 2017). This accretionary wedge was transformed into an orogenic belt during Middle Devonian as manifested by regional-scale anatexis, widespread intrusion of Circum-Pacific S-type granitoids (Jiang et al., 2016), emplacement of heterogeneous mafic rocks (e.g., Niu, Sato, et al., 2006; Wong et al., 2010), and hydrothermal mineralization (e.g., Li & Chen, 2004; Niu, Sato, et al., 2006). All these phenomena collectively point to an anomalous thermal condition that can be explained by either an abrupt change in thermal regime attributed to upwelling of hot asthenospheric mantle (e.g., Cai et al., 2010; Jiang et al., 2016; Niu, Sato, et al., 2006;

Wong et al., 2010) or subduction of an active spreading oceanic ridge (e.g., Cai et al., 2010; Jiang et al., 2010; Sun et al., 2009) or lithospheric thinning above the Pacific-type subduction systems (Jiang et al., 2016). However, this study shows that the geodynamic evolution of the Chinese Altai is far more complex than the evolution derived from the geochemistry-oriented research cited above.

The first tectonometamorphic event in the Altai wedge is undoubtedly marked by the development of the Barrovian metamorphic sequence (e.g., Burenjargal et al., 2014; Wei et al., 2007; Zhuang, 1994). It was shown above that the Barrovian index minerals grew syntectonically, parallel to the subhorizontal $S1_B$ fabric (Figures 11a–11d) during progressive increase of pressure and temperature (Figures 11k–11o and 14; see also Wei et al., 2007), compatible with tectonic burial. These results corroborate the D1 pressure increase calculated by Jiang et al. (2015) in other parts of the Chinese Altai, which suggested early moderate thickening of the Altai wedge.

Subsequent crustal extension and anatexis of the orogenic lower crust recorded by $S1_M$ are responsible for reworking of the Barrovian fabric. These data are compatible with recumbent isoclinal flow in the orogenic lower crustal rocks 100 km to the west interpreted as a result of horizontal flow of partially molten crust (Zhang et al., 2015). Formation of subhorizontal Middle Devonian sheeted granites was also reported from the lower crustal section of the neighboring Mongolian Altai (Hanžl et al., 2016; Lehmann et al., 2017). This event is associated with formation of sedimentary and volcanic Devonian basins displaying horizontal bedding and layering in rhyolite lavas in both the Chinese and Mongolian Altai (Figure 15a). Volcanic rocks dated at Middle Devonian show bimodal geochemical characteristics indicating a back-arc extensional regime (Wan et al., 2011; Xu et al., 2003). Further north, Middle Devonian sedimentary basins situated on the former Ordovician accretionary wedge were interpreted as extension-related basins based on their generally siliciclastic sedimentary infill (Soejono et al., 2018). Taken together, a significant crustal extension phase affected mainly the orogenic lower and upper crustal sections of the Altai accretionary wedge.

One major consequence of the Middle Devonian extension is regional anatexis of fertile sediments of the preexisting wedge, which could have produced a large volume of felsic melts and left a high-density mafic residue in the deep crust (Jiang et al., 2016). These authors argued that such process might cause crustal differentiation that can transform the accretionary wedge sediments into a vertically stratified and stable continental crust (Jiang et al., 2016). The extended and partially molten crust is ideally suited to develop crustal-scale doming and upright folding when submitted to horizontal compression as modeled in Lehmann et al. (2017). Using their model as a basis, we suggest that the NE-SW trending F2 folding of the crust and exhumation of partially molten rocks in the core of large antiforms (Figure 15b) were driven by a NW-SE directed shortening. Importantly, metamorphic isograds observed in the studied area are quite narrow, which can be due to the thinning of crust related to the Middle Devonian extension, or due to thinning of the limbs during postbuckle D2 flattening, or both.

It has been shown that along both modern and fossil circum-Pacific accretionary orogens, the suprasubduction domain may undergo cycles of extension and contraction (e.g., Collins, 2002; Gutscher et al., 2000). Collins (2002) proposed that the intrinsic negative buoyancy of the sinking plate accounts for the retreat of subducting slab and upper plate extension, while the intermittent arrival of buoyant oceanic plateaus could induce transient flat subduction associated to crustal thickening and orogenic contraction. This tectonic switching could induce short-lived extension-shortening cycles in orogenies (Collins, 2002). Later on, Cawood and Buchan (2007) suggested that variations of shortening and extension modes in suprasubduction setting can be controlled by global plate kinematic adjustments. This study shows a succession of tectonometamorphic and magmatic events in the Chinese Altai located above a major subduction zone in the Devonian (Xiao et al., 2009) that are compatible with the tectonic switching scenario of Collins (2002) and Collins and Richards (2008). The Chinese Altai tectonic history therefore can be interpreted as a sequence starting with an Early Devonian crustal thickening, followed by a Middle Devonian lithospheric thinning associated with melting of fertile sediments and ending with a Late Devonian doming and upright folding. In this regard, these three events may be interpreted as a result of rapid and repeated alternations of two shortening events and one extensional event during Devonian above a long-lasting subduction system.

6.3.2. Permian Deformation of the Altai Accretionary Wedge

The Permian tectonic evolution has been so far described in discrete and mutually disconnected structural, geochronological, metamorphic, and magmatic studies (Briggs et al., 2007; Li, Sun, Rosenbaum,
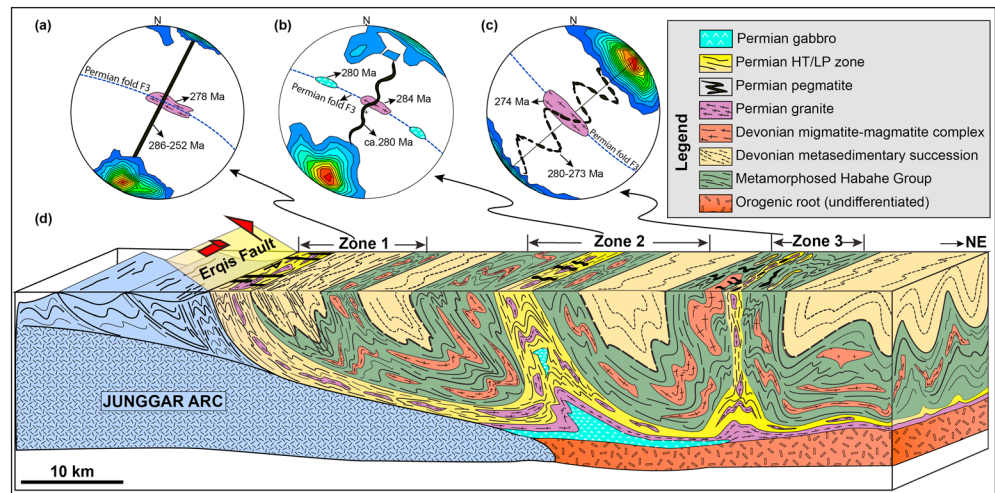
Figure 16. (a–d) Geodynamic model of the Permian collision of the Junggar arc with the Altai accretionary wedge explaining the structural evolution of three equally spaced zones in the southern Chinese Altai as a function of distance from the collisional zone in the south. Permian, ca. 280-Ma granitic and pegmatite dykes change from straight, unde-formed and nearly perpendicular to the Permian foliation in the south, to increasingly folded by Permian NW-SE folds to the north (see stereonets), suggesting that folding was already locked at that time in the south but ongoing in the north.

Cai, et al., 2016; Li et al., 2017; Tong et al., 2014; Wang et al., 2014; Zhang et al., 2012, 2014). Here we combine our structural and geochronological data with preexisting available data from the Erqis fault zone near the Fuyun city and from the Kalasu area, to propose a new model that reconciles variations of structural styles in the southern Chinese Altai and to explain the Permian geodynamic evolution of the Altai wedge.

As described above, in the Erqis fault zone to the south of the area mapped here and closer to the contact with the Junggar arc (Zone 1; Figure 2), the exposed partially molten crustal layer, dated at around 295 Ma (Li et al., 2015), has been intruded by a pegmatite dyke swarm. These dykes are undeformed and crosscut orthogonally, Permian folds and shear zones (Zone 1; Figures 16a and 16d; see also Li et al., 2017; Zhang et al., 2012). Dykes in this region were repeatedly dated by U-Pb zircon and U-Th-Pb monazite methods which yielded dominantly 286- to 277-Ma ages (Briggs et al., 2009; Gong et al., 2007) and one younger age of 252 Ma (Zhang et al., 2012). Their consistent orientation and perfect alignment suggest magma emplacement in tensional gashes (Mode I fractures), implying that the Permian ductile deformation had ended already at ca. 280 Ma and the partially molten crustal layer must have been exhumed and imbri-cated with upper crust before that time. Li et al. (2017) produced a range of high-quality ^{40}Ar/^{39}Ar single mineral ages (muscovite and biotite) ranging from 286 to 279 Ma for rocks from this southern area and inter-preted them as reflecting the timing of a main Permian transpressive deformation. We propose instead that their ages reflect the terminal stage of a Permian ductile shearing and cooling following intrusion of the Permian dyke swarm.

The Kalasu area (Zone 2; Figures 2a, 16b, and 16d), to the north of the Erqis fault zone, is characterized by a vertical and tabular deformation zone, along which ca. 299-Ma migmatites and granulites were ver-tically extruded during an important NE-SW oriented upright folding of surrounding orogenic middle and upper crust (Broussolle et al., 2018). Several granite dykes and gabbros aligned parallel to the zone of granulites-facies Permian metamorphism were dated at ca. 284–280 Ma (Broussolle et al., 2018). A large number of pegmatite dykes either crosscut or are aligned parallel to the vertical and granulite-facies deformation zone. Unlike the previous region, close to the Erqis fault zone, the pegmatite and granite dykes here are only gently folded and show a brittle cleavage refraction trending NW-SE. Here the dykes have not been yet dated so far; however, their emplacement timing can be broadly constrained at ca. 280 Ma on the basis of their syndeformational structural relationships with the high-grade tabular zone and the Permian folding (Broussolle et al., 2018). This suggests that the ductile deformation in the Kalasu area continued after emplacement and solidification of dykes as part of the late deformation dated at ca. 280 Ma (Broussolle et al., 2018).

Further north still, and away from the Erqis fault zone, in the current studied area (Zone 3; Figures 16c and 16d), the Permian event is expressed by locally distributed sillimanite-bearing HT metamorphic zone with the metamorphic age dated to ca. 299 Ma (Figure 3; see also Wang et al., 2014) and by significant crustal shortening related to our D3 NE-SW oriented superposed upright folding. This caused an intense folding of the 280- to 273-Ma pegmatite dykes emplaced in tensional fractures or failure mode I, perpendicular to the S3 cleavage, implying that the D3 deformation took place mainly during 280–273 Ma in the studied area.

In summary, these three regions, equally spaced in a northward direction, yield almost identical high-temperature metamorphic ages but exhumed diachronously. They also characterize a distinct change in the nature of deformation of the broadly contemporaneous Permian pegmatite dikes: from undeformed in the south, close to the collisional front with the Junggar arc, to intensely folded in the north, in the area investigated here. This systematic change in fold intensity favors a northward progressive model of folding, probably resulting from the Junggar-Chinese Altai collision (Li et al., 2017, and references therein). This folding process can be compared to indentation-driven fold detachment model of Lehmann et al. (2017), who applied partially molten wax-sand experiments to simulate the deformation of a crust characterized by a partially molten and thermally weak layer at depth overlain by competent material. The model shows progressive locking of detachment folds as the deformation progress, with new folds developing progressively away from the indenter (see also Blay et al., 1977). Given the similar ages of granite and pegmatite dykes across all three regions, we propose that the first folds formed in the south, adjacent to the indenter (Zone 1; Figure 16), and were already locked when the granite and pegmatite dykes were emplaced, so that the dykes intruded tensional fractures and remained undeformed. Further to the north, the same intrusion process was repeated (Zone 2; Figure 16) but the dykes were gently folded, indicating that the dykes intruded relatively late during the folding event. In our study area (Zone 3; Figure 16), in the north, the folds were actively growing at the time of dyking and dykes were tightly folded. In conclusion, the dyke swarm intruded roughly contemporaneously across the collisional zone between the Junggar arc and the Chinese Altai but the folding process was at different stages, already locked in the south, and actively folding 50 km to the north.

6.4. Implications for the Tectonic Evolution of the Mongolian Orogenic Collage

The early Paleozoic accretionary history of the Mongolian collage was considered to be initially related to a general nearly E-W convergence forming nearly N-S trending orogenic zones and structures (Lehmann et al., 2010). In their model, the final WNW-ESE orientation of CAOB belt was related to Late Carboniferous to Triassic NNE-SSW shortening associated with the formation of the Mongolian orocline (Edel et al., 2014; Guy et al., 2014; Lehmann et al., 2010) which can be attributed to the northward movement of the Tarim-North China Collage (Edel et al., 2014; Lehmann et al., 2010, 2017; Xiao et al., 2015). This shortening is coeval with the development of South Tianshan-Solonker suture and/or the collision zone along the contact of the Mongolian Collage and the Tarim-North China Collage in the south (see summary in Xiao et al., 2018).

The current study shows that in the Chinese Altai the NE-SW trending Devonian orogenic fabrics were rotated to nearly NW-SE direction due to NE-SW directed shortening during Early Permian (e.g., Zhang et al., 2015). This deformation is related with the collision of the Junggar arc with the Altai wedge, where the former behaved as a rigid indenter. The current study provides the first solid 280- to 273-Ma age constraint for this collision. In this regard, results from the present work have also major implication for onset of shortening of the whole Mongolian collage and oroclinal bending.

7. Conclusions

Structural and geochronological data presented in this paper allow constraining the geometry, kinematics, and time scales of both accretionary and collisional events which shaped the Altai accretionary wedge in NW China. The principal conclusions are as follows:

1. The Altai accretionary wedge developed a subhorizontal Barrovian-type $S1_B$ fabric as a result of moderate crustal thickening. This fabric was reactivated and reworked by partial melting resulting in the formation of high-temperature horizontal $S1_M$ in the orogenic lower crust associated with the deposition of Devonian sedimentary sequence at shallow crustal levels under an extensional regime. This stratified crust was subsequently affected by two compressive events, D2 and D3. D2 is characterized by nearly NE-SW

trending upright folding accompanied by juxtaposition of high- and low-grade metamorphic rocks. D3 is marked by nearly NE-SW shortening leading to large-scale tight folds with axes plunging SE or NW, in accordance to the limbs of F2 folds. D3 was associated with granite and pegmatite magmatism.

2. Zircon U-Pb ages indicate that the $S1_M$ horizontal fabric due to extension developed at 400–380 Ma and partly overlapped with crustal F2 folding as suggested by continuity of leucosomes in D1 and D2 structures in the orogenic lower crustal section. The NE-SW D3 convergence was active at Early Permian, at least between 280 and 273 Ma.

3. Thus, the Paleozoic geodynamic evolution of the Altai accretionary wedge is marked by Devonian tectonic switching from compression to extension and back to compression, most likely as a response to changing of subduction dynamics related to alternating slab advance and retreat. This resulted in the formation of NE-SW trending orogenic fabric that was reworked when the tectonic regime switched into the nearly NE-SW Permian shortening. The latter event is attributed to the Junggar-Chinese Altai collision involving indentation of the rigid Junggar arc domain into the weak Altai wedge, resulting in progressive detachment folding, exhumation of previously metamorphosed and thermally softened crust, and intrusion of syntectonic granite and pegmatite dykes at ca. 280 Ma across the collisional front, which recorded the advancement of the folding in front northward toward the Altai Orogenic Belt.

References

Aleinikoff, J. N., Schenck, W. S., Plank, M. O., Srogi, L., Fanning, C. M., Kamo, S. L., & Bosbyshell, H. (2006). Deciphering igneous and metamorphic events in high-grade rocks of the Wilmington Complex, Delaware: Morphology, cathodoluminescence and backscattered electron zoning, and SHRIMP U-Pb geochronology of zircon and monazite. *Geological Society of America Bulletin*, *118*(1–2), 39–64. https://doi.org/10.1130/B25659.1

Badarch, G., Dickson Cunningham, W., & Windley, B. F. (2002). A new terrane subdivision for Mongolia: Implications for the Phanerozoic crustal growth of Central Asia. *Journal of Asian Earth Sciences*, *21*(1), 87–110. https://doi.org/10.1016/S1367-9120(02)00017-2

Bureau of Geology and Mineral Resources of Xinjiang Uygur Autonomous Region (Ed) (1993). (Bureau of Geology and Mineral Resources of Xinjiang Uygur Autonomous Region) Regional Geology of Xinjiang Uygur Autonomous Region. In *People's Republic of China, ministry of geology and mineral resources*, *Geological Memoirs, Series*, (Vol. 1, No. 32, 206 pp.). Beijing: Geological Publishing House. (in Chinese)

Black, L. P., Kamo, S. L., Allen, C. M., Aleinikoff, J. N., Davis, D. W., Korsch, R. J., & Foudoulis, C. (2003). TEMORA 1: A new zircon standard for Phanerozoic U-Pb geochronology. *Chemical Geology*, *200*(1–2), 155–170. https://doi.org/10.1016/s0009-2541(03)00165-7

Blay, P., Cosgrover, J. W., & Summers, J. M. (1977). An experimental investigation of the development of structures in multilayers under the influence of gravity. *Journal of the Geological Society*, *133*(4), 329–342. https://doi.org/10.1144/gsjgs.133.4.0329

Briggs, S. M., Yin, A., Manning, C. E., Chen, Z. L., & Wang, X. F. (2009). Tectonic development of the southern Chinese Altai Range as determined by structural geology, thermobarometry, 40Ar/39Ar thermochronology, and Th/Pb ion-microprobe monazite geochronologyPermo-Triassic thrusting in the Chinese Altai. *GSA Bulletin*, *121*(9–10), 1381–1393. https://doi.org/ 10.1130/B26385.1

Briggs, S. M., Yin, A., Manning, C. E., Chen, Z. L., Wang, X. F., & Grove, M. (2007). Late Paleozoic tectonic history of the Ertix fault in the Chinese Altai and its implications for the development of the Central Asian Orogenic system. *Geological Society of America Bulletin*, *119*(7–8), 944–960. https://doi.org/10.1130/B26044.1

Broussolle, A., Aguilar, C., Sun, M., Schulmann, K., Štípská, P., Jiang, Y. D., Yu, Y., et al. (2018). Polycyclic Devonian and Permian magmatic and tectonothermal reworking of accretionary wedge in the Chinese Altai. *Lithos*, *314-315*, 400–424. https://doi.org/10.1016/j.lithos.2018.06.005

Broussolle, A., Štípská, P., Lehmann, J., Schulmann, K., Hacker, B. R., Holder, R., Kylander-Clark, A. R. C., et al. (2015). P–T–t–D record of crustal-scale horizontal flow and magma-assisted doming in the SW Mongolian Altai. *Journal of Metamorphic Geology*, *33*(4), 359–383. https://doi.org/10.1111/jmg.12124

Burenjargal, U., Okamoto, A., Kuwatani, T., Sakata, S., Hirata, T., & Tsuchiya, N. (2014). Thermal evolution of the Tseel terrane, SW Mongolia and its relation to granitoid intrusions in the Central Asian Orogenic Belt. *Journal of Metamorphic Geology*, *32*(7), 765–790. https://doi.org/10.1111/jmg.12090

Buriánek, D., Schulmann, K., Hrdličková, K., Hanžl, P., Janoušek, V., Gerdes, A., & Lexa, O. (2017). Geochemical and geochronological constraints on distinct Early-Neoproterozoic and Cambrian accretionary events along southern margin of the Baydrag Continent in western Mongolia. *Gondwana Research*, *47*(Supplement C), 200–227. https://doi.org/10.1016/j.gr.2016.09.008

Cai, K., Sun, M., Yuan, C., Long, X., & Xiao, W. (2011). Geological framework and Paleozoic tectonic history of the Chinese Altai, NW China: A review. *Russian Geology and Geophysics*, *52*(12), 1619–1633. https://doi.org/10.1016/j.rgg.2011.11.014

Cai, K., Sun, M., Yuan, C., Zhao, G., Xiao, W., Long, X., & Wu, F. (2010). Geochronological and geochemical study of mafic dykes from the northwest Chinese Altai: Implications for petrogenesis and tectonic evolution. *Gondwana Research*, *18*(4), 638–652. https://doi.org/10.1016/j.gr.2010.02.010

Cai, K., Sun, M., Yuan, C., Zhao, G., Xiao, W., Long, X., & Wu, F. (2011). Prolonged magmatism, juvenile nature and tectonic evolution of the Chinese Altai, NW China: Evidence from zircon U–Pb and Hf isotopic study of Paleozoic granitoids. *Journal of Asian Earth Sciences*, *42*(5), 949–968. https://doi.org/10.1016/j.jseaes.2010.11.020

Cawood, P. A., & Buchan, C. (2007). Linking accretionary orogenesis with supercontinent assembly. *Earth-Science Reviews*, *82*(3–4), 217–256. https://doi.org/10.1016/j.earscirev.2007.03.003

Cawood, P. A., Kröner, A., Collins, W. J., Kusky, T. M., Mooney, W. D., & Windley, B. F. (2009). Accretionary orogens through Earth history. *Geological Society, London, Special Publications*, *318*(1), 1–36. https://doi.org/10.1144/sp318.1

Chai, F., Mao, J., Dong, L., Yang, F., Liu, F., Geng, X., & Zhang, Z. (2009). Geochronology of metarhyolites from the Kangbutiebao Formation in the Kelang basin, Altay Mountains, Xinjiang: Implications for the tectonic evolution and metallogeny. *Gondwana Research*, *16*(2), 189–200. https://doi.org/10.1016/j.gr.2009.03.002

Chen, M., Sun, M., Cai, K., Buslov, M. M., Zhao, G., & Rubanova, E. S. (2014). Geochemical study of the Cambrian–Ordovician meta-sedimentary rocks from the northern Altai-Mongolian terrane, northwestern Central Asian Orogenic Belt: Implications on the provenance and tectonic setting. *Journal of Asian Earth Sciences*, *96*, 69–83. https://doi.org/10.1016/j.jseaes.2014.08.028

Christensen, N. I., & Mooney, W. D. (1995). Seismic velocity structure and composition of the continental crust: A global view. *Journal of Geophysical Research*, *100*, 9761–9788. https://doi.org/10.1029/95JB00259

Collins, W. J. (2002). Hot orogens, tectonic switching, and creation of continental crust. *Geology*, *30*(6), 535–538. https://doi.org/10.1130/0091-7613(2002)030<0535:hotsac>2.0.co;2

Collins, W. J., Belousova, E. A., Kemp, A. I. S., & Murphy, J. B. (2011). Two contrasting Phanerozoic orogenic systems revealed by hafnium isotope data. *Nature Geoscience*, *4*(5), 333–337. https://doi.org/10.1038/ngeo1127

Collins, W. J., & Richards, S. W. (2008). Geodynamic significance of S-type granites in circum-Pacific orogens. *Geology*, *36*(7), 559–562. https://doi.org/10.1130/g24658a.1

Cosgrove, J. W. (1997). The influence of mechanical anisotropy on the behaviour of the lower crust. *Tectonophysics*, *280*(1-2), 1–14. https://doi.org/10.1016/S0040-1951(97)00145-5

Donskaya, T., Sklyarov, E. V., Gladkochub, D. P., Mazukabzov, A. M., Sal'nikova, E., Kovach, V., Yakovleva, S. Z., et al. (2000). The Baikal collisional metamorphic belt. *Doklady Earth Sciences*, *374*(7), 1075–1079. (in Russian)

Ebadi, A., & Johannes, W. (1991). Beginning of melting and composition of first melts in the system Qz-Ab-Or-H$_2$O-CO$_2$. *Contributions to Mineralogy and Petrology*, *106*(3), 286–295. https://doi.org/10.1007/bf00324558

Edel, J. B., Schulmann, K., Hanžl, P., & Lexa, O. (2014). Palaeomagnetic and structural constraints on 90° anticlockwise rotation in SW Mongolia during the Permo–Triassic: Implications for Altaid oroclinal bending. Preliminary palaeomagnetic results. *Journal of Asian Earth Sciences*, *94*, 157–171. https://doi.org/10.1016/j.jseaes.2014.07.039

Gladkochub, D. P., Donskaya, T. V., Wingate, M. T. D., Poller, U., Kröner, A., Fedorovsky, V. S., Mazukabzov, A. M., et al. (2008). Petrology, geochronology, and tectonic implications of c. 500 Ma metamorphic and igneous rocks along the northern margin of the Central Asian Orogen (Olkhon terrane, Lake Baikal, Siberia). *Journal of the Geological Society*, *165*(1), 235–246. https://doi.org/10.1144/0016-76492006-125

Gong, H. L., Chen, Z. L., Hu, Y. Q., Li, L., Lai, X. R., Ma, Q. Y., et al. (2007). Geochemical characteristic of the acid dyke swarm from the eastern segment of the Eritix (Irtish) tectonic belt, Altai orogeny and its geological implications. *Acta Petrologica Sinica*, *23*(05), 889–899.

Guiraud, M., Powell, R., & Rebay, G. (2001). H$_2$O in metamorphism and unexpected behaviour in the preservation of metamorphic mineral assemblages. *Journal of Metamorphic Geology*, *19*(4), 445–454. https://doi.org/10.1046/j.0263-4929.2001.00320.x

Gutscher, M.-A., Spakman, W., Bijwaard, H., & Engdahl, E. R. (2000). Geodynamics of flat subduction: Seismicity and tomographic constraints from the Andean margin. *Tectonics*, *19*, 814–833. https://doi.org/10.1029/1999TC001152

Guy, A., Schulmann, K., Clauer, N., Hasalová, P., Seltmann, R., Armstrong, R., Lexa, O., et al. (2014). Late Paleozoic–Mesozoic tectonic evolution of the Trans-Altai and South Gobi Zones in southern Mongolia based on structural and geochronological data. *Gondwana Research*, *25*(1), 309–337. https://doi.org/10.1016/j.gr.2013.03.014

Hanžl, P., Schulmann, K., Janousek, V., Lexa, O., Hrdlickova, K., Jiang, Y., Buriánek, D., et al. (2016). Making continental crust: Origin of Devonian orthogneisses from SE Mongolian Altai. *Journal of Geosciences*, *61*(1), 25–50. https://doi.org/10.3190/jgeosci.206

Helo, C., Hegner, E., Kröner, A., Badarch, G., Tomurtogoo, O., Windley, B. F., & Dulski, P. (2006). Geochemical signature of Paleozoic accretionary complexes of the Central Asian Orogenic Belt in South Mongolia: Constraints on arc environments and crustal growth. *Chemical Geology*, *227*(3–4), 236–257. https://doi.org/10.1016/j.chemgeo.2005.10.003

Hu, Z., Zhang, W., Liu, Y., Gao, S., Li, M., Zong, K., Chen, H., et al. (2015). "Wave" signal-smoothing and mercury-removing device for laser ablation quadrupole and multiple collector ICPMS analysis: Application to lead isotope analysis. *Analytical Chemistry*, *87*(2), 1152–1157. https://doi.org/10.1021/ac503749k

Ireland, T., & Williams, I. S. (2003). Consideration in zircon geochronology by SIMS. *Reviews in Mineralogy and Geochemistry*, *53*(1), 215–241. https://doi.org/10.2113/0530215

Janoušek, V., Jiang, Y., Buriánek, D., Schulmann, K., Hanžl, P., Soejono, I., Kröner, A., et al. (2018). Cambrian–Ordovician magmatism of the Ikh-Mongol Arc System exemplified by the Khantaishir Magmatic Complex (Lake Zone, south–central Mongolia). *Gondwana Research*, *54*(supplement C), 122–149. https://doi.org/10.1016/j.gr.2017.10.003

Jeřábek, P., Lexa, O., Schulmann, K., & Plašienka, D. (2012). Inverse ductile thinning via lower crustal flow and fold-induced doming in the West Carpathian Eo-Alpine collisional wedge. *Tectonics*, *31*, TC5002. https://doi.org/10.1029/2012TC003097

Jiang, Y., Sun, M., Kröner, A., Tumurkhuu, D., Long, X., Zhao, G., Yuan, C., et al. (2012). The high-grade Tseel Terrane in SW Mongolia: An Early Paleozoic arc system or a Precambrian sliver? *Lithos*, *142-143*, 95–115. https://doi.org/10.1016/j.lithos.2012.02.016

Jiang, Y., Sun, M., Zhao, G., Yuan, C., Xiao, W., Xia, X., Long, X., et al. (2010). The ~390 Ma high-T metamorphic event in the Chinese Altai: A consequence of ridge-subduction? *American Journal of Science*, *310*(10), 1421–1452. https://doi.org/10.2475/10.2010.08

Jiang, Y., Sun, M., Zhao, G., Yuan, C., Xiao, W., Xia, X., Long, X., et al. (2011). Precambrian detrital zircons in the Early Paleozoic Chinese Altai: Their provenance and implications for the crustal growth of central Asia. *Precambrian Research*, *189*(1–2), 140–154. https://doi.org/10.1016/j.precamres.2011.05.008

Jiang, Y. D., Schulmann, K., Kröner, A., Sun, M., Lexa, O., Janoušek, V., Buriánek, D., et al. (2017). Neoproterozoic-Early Paleozoic Peri-Pacific accretionary evolution of the Mongolian collage system: Insights from geochemical and U-Pb zircon data from the Ordovician sedimentary wedge in the Mongolian Altai. *Tectonics*, *36*, 2305–2331. https://doi.org/10.1002/2017TC004533

Jiang, Y. D., Schulmann, K., Sun, M., Štípská, P., Guy, A., Janoušek, V., Lexa, O., et al. (2016). Anatexis of accretionary wedge, Pacific-type magmatism, and formation of vertically stratified continental crust in the Altai Orogenic Belt. *Tectonics*, *35*, 3095–3118. https://doi.org/10.1002/2016TC004271

Jiang, Y. D., Štípská, P., Sun, M., Schulmann, K., Zhang, J., Wu, Q. H., et al. (2015). Juxtaposition of Barrovian and migmatite domains in the Chinese Altai: A result of crustal thickening followed by doming of partially molten lower crust. *Journal of Metamorphic Geology*, *33*(1), 45–70. https://doi.org/10.1111/jmg.12110

Kröner, A., Windley, B. F., Badarch, G., Tomurtogoo, O., Hegner, E., Jahn, B. M., et al. (2007). Accretionary growth and crust formation in the Central Asian Orogenic Belt and comparison with the Arabian-Nubian shield. *Geological Society of America Memoirs*, *200*, 181–209. https://doi.org/10.1130/2007.1200(11)

Laurent-Charvet, S., Charvet, J., Monié, P., & Shu, L. (2003). Late Paleozoic strike-slip shear zones in eastern central Asia (NW China): New structural and geochronological data. *Tectonics*, *22*(2), 1009. https://doi.org/10.1029/2001TC901047

Lehmann, J., Schulmann, K., Lexa, O., Corsini, M., Kröner, A., Štípská, P., et al. (2010). Structural constraints on the evolution of the Central Asian Orogenic Belt in SW Mongolia. *American Journal of Science*, *310*(7), 575–628. https://doi.org/10.2475/07.2010.02

Lehmann, J., Schulmann, K., Lexa, O., Závada, P., Štípská, P., Hasalová, P., et al. (2017). Detachment folding of partially molten crust in accretionary orogens: A new magma-enhanced vertical mass and heat transfer mechanism. *Lithosphere*, *9*(6), 889–909. https://doi.org/10.1130/L670.1

Li, C. Y., Zhang, H., Wang, F. Y., Liu, J. Q., Sun, Y. L., Hao, X. L., et al. (2012). The formation of the Dabaoshan porphyry molybdenum deposit induced by slab rollback. *Lithos*, *150*, 101–110. https://doi.org/10.1016/j.lithos.2012.04.001

Li, H. Q., & Chen, F. W. (2004). *Isotopic geochronology of regional mineralization in Xinjiang*. NW China, Beijing: Geological Publishing House. (in Chinese)

Li, P., Sun, M., Rosenbaum, G., Cai, K., Chen, M., & He, Y. (2016). Transpressional deformation, strain partitioning and fold superimposition in the southern Chinese Altai, Central Asian Orogenic Belt. *Journal of Structural Geology*, *87*, 64–80. https://doi.org/10.1016/j.jsg.2016.04.006

Li, P., Sun, M., Rosenbaum, G., Cai, K., & Yu, Y. (2015). Structural evolution of the Irtysh Shear Zone (northwestern China) and implications for the amalgamation of arc systems in the Central Asian Orogenic Belt. *Journal of Structural Geology*, *80*, 142–156. https://doi.org/10.1016/j.jsg.2015.08.008

Li, P., Sun, M., Rosenbaum, G., Jiang, Y., & Cai, K. (2016). Structural evolution of zonal metamorphic sequences in the southern Chinese Altai and relationships to Permian transpressional tectonics in the Central Asian Orogenic Belt. *Tectonophysics*, *693*, 277–289. https://doi.org/10.1016/j.tecto.2015.11.035

Li, P., Sun, M., Rosenbaum, G., Jourdan, F., Li, S., & Cai, K. (2017). Late Paleozoic closure of the Ob-Zaisan Ocean along the Irtysh shear zone (NW China): Implications for arc amalgamation and oroclinal bending in the Central Asian orogenic belt. *Geological Society of America Bulletin*, *129*(5-6), 547–569. https://doi.org/10.1130/b31541.1

Li, X. H., Liu, Y., Li, Q. L., Guo, C. H., & Chamberlain, K. R. (2009). Precise determination of Phanerozoic zircon Pb/Pb age by multicollector SIMS without external standardization. *Geochemistry, Geophysics, Geosystems*, *10*, Q04010. https://doi.org/10.1029/2009GC002400

Li, Z., Yang, X., Li, Y., Santosh, M., Chen, H., & Xiao, W. (2014). Late Paleozoic tectono–metamorphic evolution of the Altai segment of the Central Asian Orogenic Belt: Constraints from metamorphic P–T pseudosection and zircon U–Pb dating of ultra-high-temperature granulite. *Lithos*, *204*, 83–96. https://doi.org/10.1016/j.lithos.2014.05.022

Liu, W., Liu, X. J., & Xiao, W. J. (2012). Massive granitoid production without massive continental-crust growth in the Chinese Altay: Insight into the source rock of granitoids using integrated zircon U-Pb age, Hf-Nd-Sr isotopes and geochemistry. *American Journal of Science*, *312*(6), 629–684. https://doi.org/10.2475/06.2012.02

Liu, Y., Hu, Z., Gao, S., Günther, D., Xu, J., Gao, C., & Chen, H. (2008). In situ analysis of major and trace elements of anhydrous minerals by LA-ICP-MS without applying an internal standard. *Chemical Geology*, *257*(1–2), 34–43. https://doi.org/10.1016/j.chemgeo.2008.08.004

Long, X., Sun, M., Yuan, C., Xiao, W., & Cai, K. (2008). Early Paleozoic sedimentary record of the Chinese Altai: Implications for its tectonic evolution. *Sedimentary Geology*, *208*(3–4), 88–100. https://doi.org/10.1016/j.sedgeo.2008.05.002

Mossakovsky, A. A., Ruzhentsev, S. V., Samygin, S. G., & Kheraskova, T. N. (1993). Central Asian fold belt: Geodynamic evolution and history of formation. *Geotektonicka*, *6*, 3–33(in Russia).

Nguyen, H., Hanžl, P., Janoušek, V., Schulmann, K., Ulrich, M., Jiang, Y., et al. (2018). Geochemistry and geochronology of Mississippian volcanic rocks from SW Mongolia: Implications for terrane subdivision and magmatic arc activity in the Trans-Altai Zone. *Journal of Asian Earth Sciences*, *164*, 322–343. https://doi.org/10.1016/j.jseaes.2018.06.029

Niu, H., Sato, H., Zhang, H., Ito, J. i., Yu, X., Nagao, T., et al. (2006). Juxtaposition of adakite, boninite, high-TiO_2 and low-TiO_2 basalts in the Devonian southern Altay, Xinjiang, NW China. *Journal of Asian Earth Sciences*, *28*(4–6), 439–456. https://doi.org/10.1016/j.jseaes.2005.11.010

Niu, H., Yu, X., Xu, J., Shan, Q., Chen, F., Zhang, H., & Zheng, Z. P. (2006). *Late Paleozoic volcanism and associated metallogenesis in the Altay area*. Xinjiang, China: Geological Publishing House Beijing.

Paterson, S. R., Vernon, R. H., & Tobisch, O. T. (1989). A review of criteria for the identification of magmatic and tectonic foliations in granitoids. *Journal of Structural Geology*, *11*(3), 349–363. https://doi.org/10.1016/0191-8141(89)90074-6

Safonova, I. Y., Utsunomiya, A., Kojima, S., Nakae, S., Tomurtogoo, O., Filippov, A. N., & Koizumi, K. (2009). Pacific superplume-related oceanic basalts hosted by accretionary complexes of Central Asia, Russian Far East and Japan. *Gondwana Research*, *16*(3–4), 587–608. https://doi.org/10.1016/j.gr.2009.02.008

Schulmann, K., Kröner, A., Hegner, E., Wendt, I., Konopásek, J., Lexa, O., & Štípská, P. (2005). Chronological constraints on the pre-orogenic history, burial and exhumation of deep-seated rocks along the eastern margin of the Variscan Orogen, Bohemian Massif, Czech Republic. *American Journal of Science*, *305*(5), 407–448. https://doi.org/10.2475/ajs.305.5.407

Schulmann, K., & Paterson, S. (2011). Asian continental growth. *Nature Geoscience*, *4*(12), 827. https://doi.org/10.1038/ngeo1339–829.

Şengör, A. M. C., & Natal'in, B. A. (1996). Turkic-type orogeny and its role in the making of the continental crust. *Annual Review of Earth and Planetary Sciences*, *24*(1), 263–337. https://doi.org/10.1146/annurev.earth.24.1.263.

Şengör, A. M. C., Natal'in, B. A., & Burtman, V. S. (1993). Evolution of the Altaid tectonic collage and Paleozoic crustal growth in Eurasia. *Nature*, *364*(6435), 299–307. https://doi.org/10.1038/364299a0.

Sláma, J., Kosler, J., Condon, D. J., Crowley, J. L., Gerdes, A., Hanchar, J. M., et al. (2008). Plesovice zircon—A new natural reference material for U-Pb and Hf isotopic microanalysis. *Chemical Geology*, *249*(1–2), 1–35. https://doi.org/10.1016/j.chemgeo.2007.11.005

Soejono, I., Čáp, P., Míková, J., Janoušek, V., Buriánek, D., & Schulmann, K. (2018). Early Palaeozoic sedimentary record and provenance of flysch sequences in the Hovd Zone (western Mongolia): Implications for the geodynamic evolution of the Altai accretionary wedge system. *Gondwana Research*, *64*, 163–183. https://doi.org/10.1016/j.gr.2018.07.009

Stacey, J. S., & Kramers, J. D. (1975). Approximation of terrestrial lead isotope evolution by a two-stage model. *Earth and Planetary Science Letters*, *26*(2), 207–221. https://doi.org/10.1016/0012-821X(75)90088-6

Štípská, P., Chopin, F., Skrzypek, E., Schulmann, K., Pitra, P., Lexa, O., et al. (2012). The juxtaposition of eclogite and mid-crustal rocks in the Orlica–Śnieżnik Dome, Bohemian Massif. *Journal of Metamorphic Geology*, *30*(2), 213–234. https://doi.org/10.1111/j.1525-1314.2011.00964.x

Štípská, P., Schulmann, K., & Powell, R. (2008). Contrasting metamorphic histories of lenses of high-pressure rocks and host migmatites with a flat orogenic fabric (Bohemian Massif, Czech Republic): A result of tectonic mixing within horizontal crustal flow? *Journal of Metamorphic Geology*, *26*(6), 623–646. https://doi.org/10.1111/j.1525-1314.2008.00781.x

Sun, M., Long, X., Cai, K., Jiang, Y., Wang, B., Yuan, C., et al. (2009). Early Paleozoic ridge subduction in the Chinese Altai: Insight from the abrupt change in zircon Hf isotopic compositions. *Science in China Series D-Earth Sciences*, *52*(9), 1345–1358. https://doi.org/10.1007/s11430-009-0110-3

Sun, M., Yuan, C., Xiao, W., Long, X., Xia, X., Zhao, G., et al. (2008). Zircon U-Pb and Hf isotopic study of gneissic rocks from the Chinese Altai: Progressive accretionary history in the early to middle Palaeozoic. *Chemical Geology*, *247*(3–4), 352–383. https://doi.org/10.1016/j.chemgeo.2007.10.026

Tian, Z., Xiao, W., Shan, Y., Windley, B., Han, C., Zhang, J. E., & Song, D. (2013). Mega-fold interference patterns in the Beishan orogen (NW China) created by change in plate configuration during Permo-Triassic termination of the Altaids. *Journal of Structural Geology*, *52*, 119–135. https://doi.org/10.1016/j.jsg.2013.03.016

Tong, L., Xu, Y. G., Cawood, P. A., Zhou, X., Chen, Y., & Liu, Z. (2014). Anticlockwise P–T evolution at ∼280 Ma recorded from ultrahigh-temperature metapelitic granulite in the Chinese Altai orogenic belt, a possible link with the Tarim mantle plume? *Journal of Asian Earth Sciences*, *94*, 1–11. https://doi.org/10.1016/j.jseaes.2014.07.043

Tong, L. X., Chen, Y. B., Xu, Y. G., Zhou, X., & Liu, Z. (2013). Zircon U-Pb ages of the ultrahigh-temperature metapelitic granulite from the Altai orogen, NW China, and geological implications *Acta Petrologica Sinica*, *29*(10), 3435–3445.

Tong, Y., Wang, T., Hong, D. W., Dai, Y. J., Hang, B. F., & Liu, X. M. (2007). Ages and origin of the early Devonian granites from the north part of Chinese Altai Mountains and its tectonic implications. *Acta Petrologica Sinica*, *23*(8), 1933–1944. (In Chinese)

Wan, B., Xiao, W., Zhang, L., Windley, B. F., Han, C., & Quinn, C. D. (2011). Contrasting styles of mineralization in the Chinese Altai and East Junggar, NW China: Implications for the accretionary history of the southern Altaids. *Journal of the Geological Society*, *168*(6), 1311–1321. https://doi.org/10.1144/0016-76492011-021

Wang, T., Hong, D. W., Jahn, B. M., Tong, Y., Wang, Y. B., Hang, B. F., & Wang, X.-X. (2006). Timing, Petrogenesis, and setting of Paleozoic synorogenic intrusions from the Altai Mountains, Northwest China: Implications for the tectonic evolution of an accretionary orogen. *Journal of Geology*, *114*(6), 735–751. https://doi.org/10.1086/507617

Wang, T., Jahn, B. M., Kovach, V. P., Tong, Y., Hong, D. W., & Han, B. F. (2009). Nd-Sr isotopic mapping of the Chinese Altai and implications for continental growth in the Central Asian Orogenic Belt. *Lithos*, *110*(1–4), 359–372. https://doi.org/10.1016/j.lithos.2009.02.001

Wang, W., Wei, C., Wang, T., Lou, Y., & Chu, H. (2009). Confirmation of pelitic granulite in the Altai orogen and its geological significance. *Chinese Science Bulletin*, *54*(14), 2543–2548. https://doi.org/10.1007/s11434-009-0041-6

Wang, W., Wei, C., Zhang, Y., Chu, H., Zhao, Y., & Liu, X. (2014). Age and origin of sillimanite schist from the Chinese Altai metamorphic belt: Implications for late Palaeozoic tectonic evolution of the Central Asian Orogenic Belt. *International Geology Review*, *56*(2), 224–236. https://doi.org/10.1080/00206814.2013.841335

Wei, C., Clarke, G., Tian, W., & Qiu, L. (2007). Transition of metamorphic series from the Kyanite- to andalusite-types in the Altai orogen, Xinjiang, China: Evidence from petrography and calculated KMnFMASH and KFMASH phase relations. *Lithos*, *96*(3-4. https://doi.org/10.1016/j.lithos.2006.11.004), 353–374.

Weinberg, R. F., Veveakis, E., & Regenauer-Lieb, K. (2015). Compaction-driven melt segregation in migmatites. *Geology*, *43*(6), 471–474. https://doi.org/10.1130/G36562.1

White, R. W., Powell, R., & Halpin, J. A. (2004). Spatially-focused melt formation in aluminous metapelites from Broken Hill, Australia. *Journal of Metamorphic Geology*, *22*(9), 825–845. https://doi.org/10.1111/j.1525-1314.2004.00553.x

Wilhem, C., Windley, B. F., & Stampfli, G. M. (2012). The Altaids of Central Asia: A tectonic and evolutionary innovative review. *Earth-Science Reviews*, *113*(3–4), 303–341. https://doi.org/10.1016/j.earscirev.2012.04.001

Windley, B. F., Alexeiev, D., Xiao, W. J., Kroner, A., & Basarch, G. (2007). Tectonic models for accretion of the Central Asian Orogenic Belt. *Journal of the Geological Society of London*, *164*(1), 31–47. https://doi.org/10.1144/0016-76492006-022.

Windley, B. F., Kroner, A., Guo, J., Qu, G., Li, Y., & Zhang, C. (2002). Neoproterozoic to Paleozoic geology of the Altai Orogen, NW China: New zircon age data and tectonic evolution. *The Journal of Geology*, *110*(6), 719–737. https://doi.org/10.1086/342866

Wong, K., Sun, M., Zhao, G., Yuan, C., & Xiao, W. (2010). Geochemical and geochronological studies of the Alegedayi Ophiolitic complex and its implication for the evolution of the Chinese Altai. *Gondwana Research*, *18*(2-3), 438–454. https://doi.org/10.1016/j.gr.2010.01.010.

Xiao, W., Windley, B. F., Han, C., Liu, W., Wan, B., Ao, S., Zhang, Z., et al. (2018). Late Paleozoic to early Triassic multiple roll-back and oroclinal bending of the Mongolia collage in Central Asia. *Earth-Science Reviews* https://doi.org/10.1016/j.earscirev.2017.09.020, *186*, 94–128.

Xiao, W., Windley, B. F., Sun, S., Li, J., Huang, B., Han, C., et al. (2015). A tale of amalgamation of three Permo-Triassic collage systems in Central Asia: Oroclines, sutures, and terminal accretion. *Annual Review of Earth and Planetary Sciences*, *43*(1), 477–507. https://doi.org/10.1146/annurev-earth-060614-105254

Xiao, W. J., Windley, B. F., Hao, J., & Zhai, M. G. (2003). Accretion leading to collision and the Permian Solonker suture, Inner Mongolia, China: Termination of the central Asian orogenic belt. *Tectonics*, *22*(6), 1069. https://doi.org/10.1029/2002TC001484

Xiao, W. J., Windley, B. F., Yuan, C., Sun, M., Han, C. M., Lin, S. F., et al. (2009). Paleozoic multiple subduction-accretion processes of the southern Altaids. *American Journal of Science*, *309*(3), 221–270. https://doi.org/10.2475/03.2009.02

Xu, J. F., Castillo, P. R., Chen, F. R., Niu, H. C., Yu, X. Y., & Zhen, Z. P. (2003). Geochemistry of late Paleozoic mafic igneous rocks from the Kuerti area, Xinjiang, northwest China: Implications for backarc mantle evolution. *Chemical Geology*, *193*(1–2), 137–154. https://doi.org/10.1016/S0009-2541(02)00265-6

Yuan, C., Sun, M., Xiao, W., Li, X., Chen, H., Lin, S., et al. (2007). Accretionary orogenesis of the Chinese Altai: Insights from Paleozoic granitoids. *Chemical Geology*, *242*(1–2), 22–39. https://doi.org/10.1016/j.chemgeo.2007.02.013

Závada, P., Schulmann, K., Racek, M., Hasalová, P., Jeřábek, P., Weinberg, R. F., et al. (2018). Role of strain localization and melt flow on exhumation of deeply subducted continental crust. *Lithosphere*, *10*(2), 217–238. https://doi.org/10.1130/L666.1

Zhang, C. L., Santosh, M., Zou, H. B., Xu, Y. G., Zhou, G., Dong, Y. G., et al. (2012). Revisiting the "Irtish tectonic belt": Implications for the Paleozoic tectonic evolution of the Altai orogen. *Journal of Asian Earth Sciences*, *52*, 117–133. https://doi.org/10.1016/j.jseaes.2012.02.016

Zhang, C. L., Zou, H. B., Yao, C. Y., & Dong, Y. G. (2014). Origin of Permian gabbroic intrusions in the southern margin of the Altai Orogenic belt: A possible link to the Permian Tarim mantle plume? *Lithos*, *204*, 112–124. https://doi.org/10.1016/j.lithos.2014.05.019

Zhang, J., Sun, M., Schulmann, K., Zhao, G., Wu, Q., Jiang, Y., et al. (2015). Distinct deformational history of two contrasting tectonic domains in the Chinese Altai: Their significance in understanding accretionary orogenic process. *Journal of Structural Geology*, *73*, 64–82. https://doi.org/10.1016/j.jsg.2015.02.007

Zheng, C., Takenori, K., Masaki, E., & Cuechun, X. (2007). CHIME monazite ages of metasediments from the Altai orogen in northwestern China: Devonian and Permian ages of metamorphism and their significance. *Island Arc*, *16*(4), 598–604. https://doi.org/10.1111/j.1440-1738.2007.00585.x

Zhuang, Y. (1994). The perssure-temperature-space-time (*P-T-S-t*) evolution of metamorphism and development mechanism of the thermal-structural-gneiss domes in the Chinese Altaides. *Acta Geologica Sinica*, *68*(1), 35–47. (in Chinese)

Zou, T. R., Cao, H. Z., & Wu, B. Q. (1988). Orogenic or anorogenic granitoids of the Altay Mountains, Xinjiang and their discrimination criteria. *Acta Geologica Sinica*, *62*, 228–245. (in Chinese)